Ribosome–Mitochondria Coupling Defines Translational Capacity as a Limiting Determinant of Cardiac Metabolic Output

Xiaofang Zhang[1†], Qiaxin Xu[1,2†], Haowen Ye[3†], Shishi Li[1], Jiaxin Wang[1], Tianqi Duo[1], Na Wang[1], Luchen Shan[2], Wenyue Li[1], Jiali Fu[1], Jingde Han[1], Zhou Yang [1], Yanjie Lu[1,4,5], Jun Guo[3]*, Baofeng Yang[4]*, Jinghao Wang[1,5]*, Zhiguo Wang[1]*

[1]Department of Pharmacy, Guangdong Provincial Key Laboratory for Mechanistic and Translational Research on Chronic Disease Interactions, Academician Collaborative Laboratory for Basic Research and Translation of Chronic Diseases, the First Affiliated Hospital of Jinan University, Jinan University, Guangzhou, Guangdong 510630, China
[2]School of Pharmacy, Jinan University, Guangzhou, Guangdong, 511436, China
[3]Department of Cardiology, the First Clinical Medical College of Jinan University School of Medicine, Jinan University, Guangzhou, Guangdong 510630, China
[4]State Key Laboratory of Frigid Zone Cardiovascular Diseases (SKLFZCD), Department of Pharmacology (State Key Laboratory of Frigid Zone Cardiovascular Diseases, State-Province Key Laboratories of Biomedicine-Pharmaceutics of China, Key Laboratory of Cardiovascular Medicine Research, Ministry of Education), College of Pharmacy, Harbin Medical University, Harbin 150081, China
[5]State Key Laboratory of Bioactive Molecules and Druggability Assessment, Guangdong Basic Research Center of Excellence for Natural Bioactive Molecules and Discovery of Innovative Drugs, College of Pharmacy, Jinan University

[†]Authors with equal contributions
***Corresponding authors:** dr.guojun@163.com (J Guo); yangbf@ems.hrbmu.edu.cn (BF Yang); wangjinghao@jnu.edu.cn (J Wang); wangzhiguo@ext.jnu.edu.cn (Z Wang)

Graphical Abstract

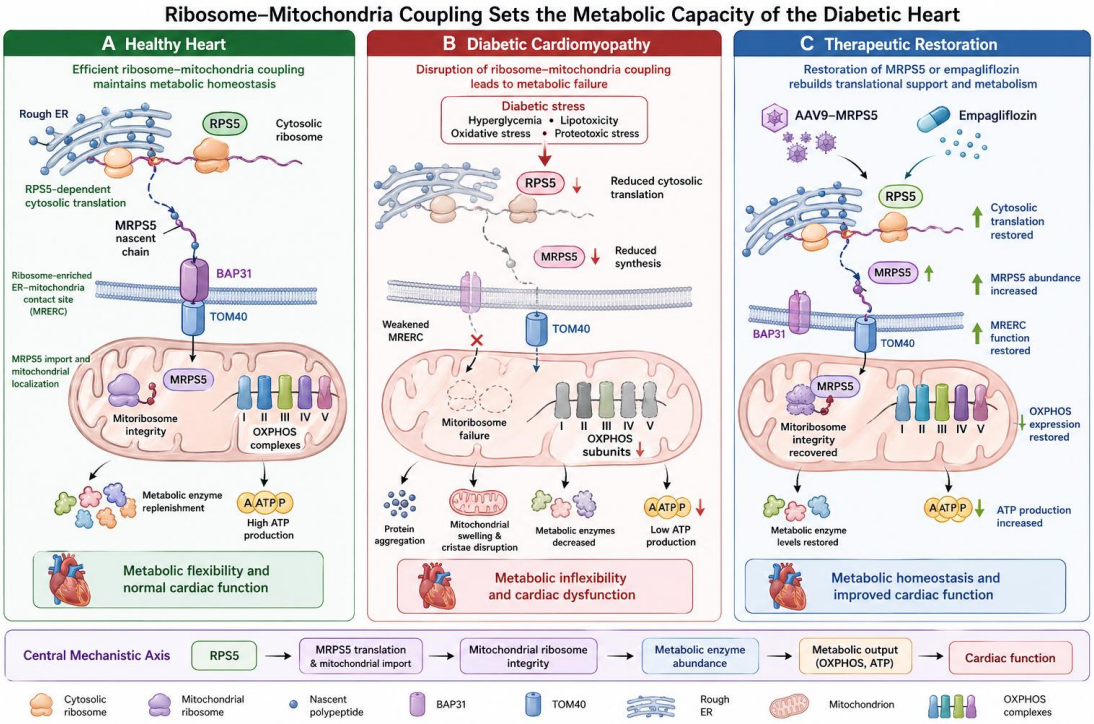

Graphical Abstract Caption: Model of ribosome–mitochondria coupling as a determinant of cardiac metabolic output in diabetic cardiomyopathy. In healthy cardiomyocytes, cytosolic translational machinery containing RPS5 supports MRPS5 production and facilitates its mitochondrial localization through ribosome-enriched ER–mitochondria contact regions involving BAP31 and TOM40. Efficient MRPS5 import preserves mitochondrial ribosome integrity, oxidative phosphorylation protein expression, metabolic enzyme replenishment, and ATP production. Under diabetic stress, coordinated downregulation of RPS5 and MRPS5 disrupts this ribosome–mitochondria coupling mechanism, leading to impaired mitochondrial translation, proteostasis collapse, reduced metabolic enzyme abundance, mitochondrial dysfunction, and cardiac contractile impairment. Restoration of MRPS5 or empagliflozin treatment partially reconstitutes translational support for mitochondrial metabolism, improves metabolic homeostasis, preserves mitochondrial ultrastructure, and enhances cardiac performance.

Highlights

- Translational capacity is reduced in the diabetic heart and correlates with metabolic dysfunction.
- RPS5 and MRPS5 are coordinately downregulated and define a translational module.
- RPS5 promotes MRPS5 protein expression and mitochondrial localization.
- Disruption of the RPS5–MRPS5 axis is associated with impaired mitochondrial metabolism.
- Restoration of MRPS5 improves mitochondrial function and cardiac performance in vivo.

In Brief

The diabetic heart exhibits impaired protein synthesis that coincides with reduced metabolic capacity. Our team identify a ribosome–mitochondria coupling mechanism in which RPS5 supports MRPS5 expression and mitochondrial function, linking translational capacity to metabolic homeostasis.

Summary

Metabolic homeostasis requires continuous synthesis of enzymes and organellar components, yet whether biosynthetic capacity constrains metabolic function remains unclear. Here, we show that translational capacity is impaired in the diabetic heart and is associated with reduced metabolic performance. Integrated transcriptomic and proteomic analyses reveal widespread discordance between mRNA and protein abundance, consistent with a dominant role for post-transcriptional regulation. We identify coordinated downregulation of the cytosolic ribosomal protein RPS5 and the mitochondrial ribosomal protein MRPS5 as a key feature of this state. RPS5 promotes MRPS5 protein production and supports its mitochondrial localization, linking cytosolic translation to mitochondrial protein synthesis. Disruption of this axis is associated with reduced abundance of metabolic enzymes and impaired oxidative metabolism, whereas restoration of either RPS5 or MRPS5 alone improves mitochondrial and cardiac function in vivo. These findings support a model in which translational capacity contributes to the maintenance of metabolic homeostasis and identify ribosome–mitochondria coupling as a mechanism coordinating protein synthesis with mitochondrial function in the diabetic heart.

Abstract

The mechanisms that define the metabolic capacity of the heart remain incompletely understood. Here, we identify translational capacity as a rate-limiting determinant of cardiac metabolic output, mediated by a ribosome–mitochondria coupling axis linking cytosolic and mitochondrial protein synthesis. Integrated transcriptomic and proteomic analyses reveal extensive discordance between mRNA and protein abundance, accompanied by suppression of global protein synthesis, reduced ribosome biogenesis, and disruption of proteostasis. We identify a ribosome–mitochondria coupling axis in which the cytosolic ribosomal protein RPS5 regulates the abundance and mitochondrial localization of MRPS5, a component of the mitochondrial ribosome. This process occurs in association with endoplasmic reticulum–mitochondria contact sites and links cytosolic translation to mitochondrial protein synthesis. Perturbation of this axis is associated with reduced expression of metabolic enzymes and impaired mitochondrial function. Conversely, restoration of RPS5 or MRPS5 improves mitochondrial activity and cardiac performance in vivo. These findings suggest that translational capacity contributes to metabolic homeostasis and reveal a spatially organized mechanism linking protein synthesis to mitochondrial function in the diabetic heart.

Keywords: diabetic cardiomyopathy, proteostasis, ribosomal proteins (RPS5/MRPS5), mitochondrial function, metabolic homeostasis, BAP31–Tom40, mitochondria–rough endoplasmic reticulum contact sites

Introduction

Metabolic homeostasis in the heart depends on the coordinated regulation of substrate utilization, enzymatic activity, and mitochondrial function. Given the high energetic demand of cardiomyocytes, continuous synthesis of metabolic enzymes and mitochondrial proteins is required to sustain contractile function and adaptive capacity [1,2]. While transcriptional and signaling networks governing cardiac metabolism have been extensively characterized, whether the capacity to produce these proteins itself constrains metabolic function remains unclear.

Diabetic cardiomyopathy (DCM) is characterized by impaired metabolic flexibility, mitochondrial dysfunction, and energetic insufficiency[3-6]. These alterations have largely been attributed to dysregulated substrate utilization and maladaptive signaling pathways, including disruption of glucose–fatty acid cycling[7]. However, metabolic dysfunction in the diabetic heart often persists despite partial normalization of systemic metabolic parameters, suggesting that additional cell-intrinsic mechanisms may limit metabolic capacity[8,9].

Protein synthesis represents a central determinant of cellular biosynthetic capacity [10-12]. Ribosomes are increasingly recognized as dynamic regulators of gene expression, and perturbations in translational control have been linked to defects in proteostasis, mitochondrial function, and metabolic adaptation[13-15]. In particular, the abundance of cellular proteins is only partially explained by transcript levels, indicating that post-transcriptional mechanisms play a major role in shaping metabolic phenotypes. An emerging concept in metabolic biology is that metabolic homeostasis depends not only on substrate availability and enzymatic regulation, but also on the cell's capacity to continuously produce metabolic machinery such as enzymes and organellar components[11,12]. In highly energy-demanding tissues such as the heart, metabolic enzymes and mitochondrial proteins exhibit high turnover rates and require sustained biosynthesis to maintain metabolic output and flexibility[13-17]. Failure of this production capacity would be expected to impose a global constraint on metabolism, regardless of substrate supply. Yet whether impaired translational capacity contributes directly to metabolic dysfunction in the heart has not been established.

Protein synthesis represents the most proximal determinant of cellular production capacity and proteostasis and is orchestrated by ribosomes. Beyond their canonical role as passive translational machines, ribosomes are increasingly recognized as dynamically regulated entities whose composition, abundance, and activity can shape selective translation programs under physiological and pathological conditions[16-18]. Mitochondrial function further depends on coordinated expression of nuclear-encoded and mitochondrial-encoded proteins. While cytosolic ribosomes synthesize the majority of mitochondrial proteins, mitochondrial ribosomes are responsible for translating essential components of the oxidative phosphorylation machinery encoded by mitochondrial DNA[19-23]. Perturbations in ribosomal proteins or ribosome biogenesis have been linked to proteostasis failure, mitochondrial dysfunction, and impaired metabolic adaptation across multiple tissues[13,18,19-23]. The mechanisms that couple these processes under physiological and pathological conditions remain incompletely understood.

Cardiac metabolism further relies on tight coordination between cytosolic and mitochondrial protein synthesis. While cytosolic ribosomes generate mitochondrial ribosomes and the majority of metabolic enzymes, mitochondrial ribosomes are essential for the synthesis of oxidative phosphorylation components encoded by the mitochondrial genome[24-29]. Disruption of either translational system can compromise energy production and cardiac function[24-29]. However, whether cytosolic and

mitochondrial translation are coordinately regulated and whether failure of such coordination constrains metabolic capacity in DCM remain unknown. A collapse of coordinated cytosolic–mitochondrial translation would be expected to directly link proteostasis failure to mitochondrial dysfunction and global metabolic impairment.

Endoplasmic reticulum–mitochondria contact sites (MERCs) function as key interfaces for organelle communication[30-36], supporting lipid exchange, calcium signaling, and metabolic regulation. These structures have also been implicated in protein targeting and mitochondrial import[37], raising the possibility that they may provide a spatial platform for coordinating protein synthesis with mitochondrial demand. Whether translational processes are organized at these sites to support mitochondrial function is not known.

Here, we test whether impaired translational capacity contributes to metabolic dysfunction in the diabetic heart. We identify coordinated downregulation of the cytosolic ribosomal protein RPS5[38-40] and its mitochondrial homolog MRPS5[18,41-45] and uncover a spatial mechanism underlying this coordination. Functionally specialized endoplasmic reticulum–mitochondria contact regions facilitate MRPS5 biogenesis and its import into mitochondria through a BAP31–Tom40–dependent pathway[33,46-49]. Restoration of the RPS5–MRPS5 module reinstates translational support for metabolic capacity, rescues mitochondrial function, and improves cardiac performance in diabetic models. Together, these findings reposition ribosomal integrity and translational production capacity as fundamental determinants of cardiac metabolic homeostasis. We therefore hypothesized that translational capacity functions as an upstream constraint on metabolic network output. To test this, we investigated whether coupling between cytosolic and mitochondrial ribosomes governs mitochondrial proteostasis and cardiac metabolism in diabetic cardiomyopathy.

Results

Failure of Translational Capacity Disrupts Metabolism in the Diabetic Heart as Revealed by Multi-Omics Profiling

Integrated multi-omics analyses revealed that diabetic cardiomyopathy (DCM) is characterized by profound metabolic pathway disturbances tied to proteostatic failure. In hearts from diabetic mice, combined metabolomic and proteomic profiling showed significant enrichment of altered glucose, lipid, and amino acid metabolic pathways.

Proteomic KEGG pathway analysis revealed that diabetic cardiomyopathy was associated with broad suppression of metabolic pathways, accompanied by alterations in signaling and stress-related processes (**Fig. 1A**). Notably, canonical metabolic pathways, including arginine and proline metabolism, glutathione metabolism, and global metabolic pathways, were among the most significantly enriched and downregulated categories, consistent with impaired metabolic capacity in the diabetic heart. In parallel, pathways related to AMPK signaling and glucagon signaling, which are central to energy sensing and metabolic adaptation, were also significantly affected. In contrast, several non-metabolic pathways, including cytoskeletal organization, fluid shear stress and atherosclerosis, and chemical carcinogenesis–DNA adducts, were enriched, suggesting activation of stress and structural remodeling programs. Collectively, these data indicate that DCM is characterized by a coordinated decline in core metabolic pathways, particularly those related to proteostasis, alongside compensatory activation of stress-responsive signaling networks, supporting a global reprogramming of the cardiac proteome.

Gene Ontology (GO) enrichment analysis of differentially expressed proteins in DCM hearts compared to controls reveals that metabolic processes dominate the BP

category, whereas enrichment of ribonucleoprotein complex, endoplasmic reticulum membrane, and mitochondrial membrane components indicates coordinated alterations in protein synthesis and organelle homeostasis (**Fig. 1B**).

Metabolites in these pathways were markedly perturbed: for example, diabetic hearts accumulated long-chain acylcarnitines and branched-chain amino acids while showing depletion of tricarboxylic acid (TCA) cycle intermediates, indicating a bottleneck in oxidative metabolism (**Fig. 1C, D**). Consistently, proteomic analysis revealed widespread changes in metabolic enzymes. Key enzymes governing fuel utilization were downregulated in DCM hearts, including hexokinase 1 (HK1) in glycolysis, dihydrolipoamide S-acetyltransferase (DLAT) in pyruvate oxidation, glycerol-3-phosphate dehydrogenase 1 (GPD1) in glycerol metabolism, acyl-CoA oxidase 1 (ACOX1) in peroxisomal fatty acid oxidation, glucokinase (GK), as well as indoleamine 2,3-dioxygenase 1 (IDO1) and fumarylacetoacetate hydrolase (FAH) in amino acid metabolism (**Fig. 1E**). In stark contrast, transcriptomic profiling of the same hearts showed relatively minor changes in metabolic pathways; instead, mRNA changes were enriched for inflammatory and extracellular matrix pathways (**Fig. 1F**). While metabolic pathways are less prominently enriched at the transcript level, pathways related to ribosome function, inflammatory signaling (including TNF and IL-17 signaling), immune responses, and stress-associated pathways are significantly represented.

Together, these findings indicate broad metabolic remodeling accompanied by ribosome-associated alterations and suggest that post-transcriptional mechanisms may contribute to metabolic dysfunction in the diabetic heart.

Ribosome-Centered Collapse of Translational Capacity Underlies Transcriptome–Proteome Discordance in Diabetic Cardiomyopathy

To define the molecular basis of gene expression dysregulation in DCM, we performed integrated transcriptomic and proteomic analyses of cardiac tissue. Despite extensive remodeling at both levels, global correlation between mRNA and protein abundance was negligible (Pearson's $r = 0.03$), revealing a profound decoupling between transcriptional output and protein expression (**Fig. 2A**). Notably, only a small subset of shared entities exhibited concordant regulation, whereas the majority displayed discordant or uncoupled behavior, suggesting dominant post-transcriptional control. These data suggested that the metabolic deficits in DCM stem not from a lack of transcripts or substrates, but from a failure in translational capacity to produce necessary metabolic proteins.

To directly assess translational activity, we measured nascent protein synthesis using puromycin incorporation. Diabetic cardiomyocytes exhibited a marked reduction in global translation rates (**Fig. 2B**), indicating that impaired protein synthesis is a central feature of DCM.

Given that translational capacity is critically dependent on ribosome abundance, we next examined total RNA content, which is predominantly composed of ribosomal RNA. Strikingly, diabetic cardiomyocytes displayed a substantial reduction in total RNA, accompanied by diminished and poorly resolved 28S and 18S rRNA bands (**Fig. 2C**). These findings are consistent with impaired ribosome biogenesis and/or increased rRNA instability, pointing to a collapse of ribosomal capacity rather than a generalized suppression of transcription.

Ultrastructural analysis further supported this model. Transmission electron microscopy (TEM) revealed that in normal mouse cardiomyocytes, the rough endoplasmic reticulum (RER) exhibited intact structural integrity with ribosomes attached and maintained close contact with mitochondria (**Fig. 2D, left panels**). In

contrast, in diabetic cardiomyocytes, the RER lost its structural integrity, displaying swelling and dilation of the RER cisternae, partial detachment of ribosomes from the membrane, and reduced contact with mitochondria, characterized by increased inter-organellar distance (**Fig. 2D, right panels**). In parallel, ER network integrity was compromised, as evidenced by fragmentation and loss of tubular continuity (**Fig. 2E**). These structural defects indicate failure of the ER-associated translational machinery.

eIF2α is the gatekeeper of translation initiation for start codon recognition and formation of the translation initiation complex: unphosphorylated eIF2α supports protein synthesis, while phosphorylated eIF2α suppresses global translation and redirects translation toward stress-response programs[50,51]. Sec61β, a component of the Sec61 ER translocon complex, was used as a marker of ER membrane architecture to assess stress-induced remodeling of the rough ER network[52,53]. At the signaling level, diabetic cardiomyocytes exhibited robust activation of the integrated stress response, with increased phosphorylation of eIF2α (eukaryotic initiation factor 2 alpha) and its colocalization with Sec61β to rough ER-associated translation sites (**Fig. 2F**). The results are consistent with global translational repression in response to proteotoxic stress.

Functionally, these defects were accompanied by a collapse of proteostasis. Diabetic cardiomyocytes accumulated abundant protein aggregates, as detected by Thioflavin T (ThT) staining (**Fig. 2G**) and exhibited activation of unfolded protein response pathways (**Fig. 2H**). Concurrently, autophagic flux was impaired, as indicated by increased LC3B-II/I ratio and p62 accumulation (**Fig. 2I–J**), suggesting defective clearance of misfolded proteins[58,59].

Together, these data support a model in which diabetic stress induces a ribosome-centered collapse of translational capacity, driven by impaired ribosome biogenesis, structural disruption of the ER, and activation of stress-responsive translational repression pathways. This results in a failure to maintain proteome integrity, leading to widespread protein misfolding and aggregation. Importantly, this mechanism provides a unifying explanation for the observed discordance between transcriptomic and proteomic regulation, as mRNA abundance becomes uncoupled from protein synthesis in the context of translational insufficiency.

Coordinated Downregulation of RPS5 and MRPS5 Drives Proteostasis Collapse and Rescue by SGLT2 Inhibitor Empagliflozin

We next searched for specific molecular drivers of this translational failure. The running enrichment score plot of transcriptomic data indicates global suppression of ribosomal components and translational machinery in the diabetic myocardium (**Fig. 3A-C** & **Fig. 1F**). Among altered ribosomal proteins, RPS5 (a core protein of the 40S cytosolic ribosome) and MRPS5 (a core protein of the 40S cytosolic ribosome) were prioritized because they were consistently reduced across independent datasets and represent cytosolic and mitochondrial translational compartments, respectively, as determined by proteomics and confirmed by Western blots (**Fig. 3A, B**). Similarly, cultured cardiomyocytes exposed to HG+PA showed significant loss of RPS5 and MRPS5 protein compared to normal conditions (**Fig. 3C**). This coordinated downregulation suggests a failure of a ribosomal module spanning the cytosol and mitochondria. We therefore hypothesized that coordinated disruption of this pair might impair cross-compartment protein homeostasis.

In line with that, we found that MRPS5's normal localization to mitochondria was severely impaired in diabetic cardiomyocytes: immunofluorescence showed reduced mitochondrial MRPS5 signal and mislocalization of MRPS5 away from the organelle under diabetic stress (**Fig. 3D**). Notably, diabetic mice remained hyperglycemic despite

cardiac MRPS5 overexpression, and blood glucose levels were statistically indistinguishable between MRPS5-treated and untreated diabetic groups (**Fig. 3E, F**). Thus, the improved cardiac metabolism and function cannot be attributed to better blood sugar control; rather, they stem directly from enhanced cardiac translational capacity.

Intriguingly, we found that empagliflozin, an SGLT2 inhibitor with established cardiovascular benefits, robustly restored both RPS5 and MRPS5 protein levels in diabetic hearts (**Fig. 3G, H**). Consistent with restoration of RPS5/MRPS5 expression, empagliflozin also conferred marked functional and ultrastructural benefits in diabetic hearts. Representative echocardiographic recordings demonstrated improved left ventricular contractile performance and transmitral filling dynamics in empagliflozin-treated DCM mice compared with untreated DCM controls (**Fig. 3I**). Quantitative analysis confirmed that empagliflozin significantly increased ejection fraction (EF) and fractional shortening (FS), indicating recovery of systolic function, while the elevated E/A ratio further suggested amelioration of diastolic dysfunction (**Fig. 3J**). At the subcellular level, transmission electron microscopy revealed profound mitochondrial abnormalities in DCM myocardium, characterized by swelling, loss of structural integrity, and disrupted cristae organization. In contrast, empagliflozin treatment largely preserved mitochondrial ultrastructure, with mitochondria appearing more compact and displaying denser, better-organized cristae architecture (**Fig. 3K**). These findings indicate that empagliflozin not only rescues ribosomal protein deficiency but also improves cardiac performance and mitochondrial quality in diabetic cardiomyopathy. These pharmacological observations provide independent evidence that the RPS5-MRPS5 module is responsive to cardioprotective interventions and further supports its role as a nodal point in the regulation of cardiac translational capacity.

Together, the in vivo results firmly establish that translational insufficiency is a causal, reversible factor in diabetic cardiomyopathy. By reinstating the RPS5/MRPS5 proteostatic module (in this case via MRPS5), we can rescue mitochondrial integrity, normalize metabolic enzyme production, rebalance metabolism, and significantly improve cardiac performance, all without altering the external metabolic milieu. This underscores translational capacity as a key therapeutic target for DCM.

The RPS5/MRPS5 Ribosomal Module Controls Proteostasis Stress and Protein Aggregation

To further test whether restoring the ribosomal module could rescue proteostasis, we overexpressed RPS5 or MRPS5 in diabetic cardiomyocytes. Overexpression plasmids were used to elevate RPS5 or MRPS5 expression in HG+PA-treated cells, and successful overexpression was confirmed by immunoblotting (**Fig. S1A, B**). Restoration of either RPS5 or MRPS5 markedly improved proteostasis under diabetic stress. Proteotoxic stress markers[60-63] induced by HG+PA treatment were significantly attenuated following RPS5 or MRPS5 overexpression. Specifically, the elevations in HSP60, BiP, phospho-PERK, ATF4, CHOP, and LONP1 were substantially reduced, with several markers returning toward baseline levels (**Fig. 4A, B**). Quantitative analyses showed that CHOP and BiP protein levels were decreased by approximately 30%–50% relative to untreated diabetic cells ($p<0.05$). Restoring RPS5 or MRPS5 also preserved ER architecture. Overexpressing cells displayed a more continuous reticular rough ER network compared with the fragmented ER morphology observed under diabetic conditions (**Fig. 4C, D**). Concurrently, protein aggregate load was relieved, as evidenced by Thioflavin T staining showing an approximately 60% decrease in

misfolded protein deposits in RPS5- or MRPS5-overexpressing cells (p<0.01), indicating far fewer aggregates (p<0.01; **Fig. 4E, F**).

Conversely, knockdown of RPS5 or MRPS5 further aggravated proteostasis failure under diabetic stress. Using siRNA to acutely reduce RPS5 or MRPS5 expression (**Fig. S1C, D**), we observed an exacerbation of all the pathological markers. HG+PA-treated cardiomyocytes with RPS5/MRPS5 knockdown exhibited even higher levels of stress and damage than HG+PA alone. Upon RPS5/MRPS5 loss, stress response proteins were further induced: for example, CHOP and ATF4 levels were higher than in diabetic conditions alone **(Fig. 5A, B)**. ER organization deteriorated further, with more pronounced RER fragmentation and swelling **(Fig. 5C, D)**. Protein aggre

gates accumulated to even greater levels, as Thioflavin T fluorescence intensified beyond that of diabetic controls **(Fig. 5E, F)**. These trends were consistent across multiple experiments (p<0.05 for knockdown exacerbation vs. HG+PA alone).

To validate the efficiency of in vivo manipulation of ribosomal components, we next examined cardiac-specific overexpression and knockdown of RPS5 and MRPS5 in mouse hearts under basal conditions. AAV9-mediated delivery resulted in robust upregulation of RPS5 and MRPS5 protein levels in the myocardium, as confirmed by immunoblot analysis (**Fig. S1E, F**). Conversely, cardiomyocyte-specific knockdown using RNA interference effectively reduced the expression of both RPS5 and MRPS5 in vivo (**Fig. S1G, H**). These data demonstrate that our experimental system enables efficient and bidirectional modulation of cytosolic and mitochondrial ribosomal proteins in the heart, providing a reliable platform for subsequent functional studies.

Taken together, the loss-of-function and gain-of-function data together establish causality: the coordinated downregulation of RPS5 and MRPS5 in the diabetic heart is a key driver of translational insufficiency and proteostasis collapse, while restoring either component of this ribosomal module can rebuild proteostatic capacity. The failure of this RPS5–MRPS5 module under diabetic conditions therefore appears to underlie the inability of the heart to meet its protein production demands.

The RPS5–MRPS5 Translational Module Controls Metabolic Enzyme Production

We next asked whether the RPS5/MRPS5 ribosomal defect could explain the metabolic enzyme deficits in DCM. If translational capacity is limiting, then augmenting it should restore metabolic proteins. Indeed, overexpression of RPS5 led to broad upregulation of metabolic enzymes across multiple pathways in diabetic cardiomyocytes. In glucose metabolism, RPS5 restoration increased the abundance of hexokinase 1 (HK1), the enzymes that catalyze the first step of glycolysis to regulate glucose entry into metabolism **(Fig. 6A)**. These glycolytic enzymes were deficient under diabetic conditions, but their levels rose back toward normal with RPS5 overexpression. RPS5 also significantly elevated glucose-6-phosphate dehydrogenase (G6PD), the rate-limiting enzyme of the pentose phosphate pathway (critical for NADPH production and redox balance), as well as fructose-1,6-bisphosphatase 2 (FBP2), which helps regulate the glycolysis/gluconeogenesis balance in the heart.

Improvements were not limited to glucose pathways. In lipid metabolism, RPS5 overexpression increased carnitine palmitoyltransferase 2 (CPT2), essential for mitochondrial fatty acid β-oxidation; glycerol-3-phosphate dehydrogenase 1 (GPD1), which plays a key role in the glycerophosphate shuttle and triglyceride synthesis; and acyl-CoA oxidase 1 (ACOX1), the rate-limiting enzyme of peroxisomal fatty acid oxidation (**Fig. 6B**). This suggests enhanced capacity for both mitochondrial and peroxisomal fatty acid catabolism when translational capacity is restored.

Likewise, enzymes in amino acid and ancillary pathways were upregulated: RPS5 raised levels of indoleamine 2,3-dioxygenase 1 (IDO1), which initiates tryptophan catabolism via the kynurenine pathway; fumarylacetoacetate hydrolase (FAH), a TCA cycle enzyme linking amino acid breakdown to energy production; and hydroxyacyl-CoA dehydrogenase (HADH), involved in the catabolism of branched-chain amino acids such as valine, leucine, and isoleucine (**Fig. 6C**). Crucially, the opposite pattern was observed when RPS5 was knocked down. All the aforementioned metabolic enzymes fell in abundance with RPS5 silencing under diabetic conditions (**Fig. 6D-F**). For instance, HK1, CPT2, and FAH levels were further reduced (often to <50% of diabetic controls) when RPS5 was depleted, directly demonstrating a dependence of these metabolic proteins on translational capacity.

On the other hand, MRPS5 manipulation produced the same outcomes: overexpressing MRPS5 increased the same sets of enzymes (**Fig. 6G-I**) and knocking down MRPS5 decreased them in parallel (**Fig. 6J-L**). The effects of MRPS5 gain- or loss-of-function were indistinguishable from those of RPS5, underscoring that RPS5 and MRPS5 function as a unified translational module. In sum, **Figure 6** shows that this ribosome-centered module controls the protein expression of critical metabolic pathways. When the module fails (as in DCM), enzymes across glucose, lipid, and amino acid metabolism are coordinately downregulated, constraining metabolic capacity. Conversely, restoring the module drives a concerted upregulation of metabolic proteins, essentially reprogramming the metabolic proteome back toward a healthy state. These findings tie the collapse of proteostasis directly to the metabolic inflexibility of the diabetic heart: translational insufficiency in RPS5/MRPS5 translates to multi-pathway metabolic enzyme deficits.

Ribosomal Impairment Compromises Mitochondrial Integrity and Oxidative Capacity

Because the heart's energy output depends heavily on mitochondrial function, we examined how the RPS5/MRPS5 translational module influences mitochondrial integrity. In HG+PA-treated cardiomyocytes, overexpression of RPS5 or MRPS5 preserved mitochondrial membrane potential ($\Delta\Psi m$). Diabetic stress normally depolarized mitochondria (reducing the JC-1 red/green fluorescence ratio by ~30%), but RPS5 or MRPS5 overexpression prevented this loss of $\Delta\Psi m$ (**Fig. S2A, B**). Likewise, RPS5/MRPS5 restoration blunted oxidative stress: overexpressing either protein led to ~40% lower cellular reactive oxygen species (ROS) levels compared to diabetic cells ($p<0.01$), as measured by DCF fluorescence (**Fig. S2C, D**). Thus, boosting translational capacity helped maintain mitochondrial polarization and limited ROS accumulation under diabetic conditions.

Importantly, mitochondrial respiratory machinery was also preserved. Western blots showed that RPS5 or MRPS5 overexpression restored the protein abundance of multiple oxidative phosphorylation (OXPHOS) complex subunits that were otherwise depressed by diabetes, including NDUFB8 (Complex I)**,** SDHB (Complex II)**,** UQCRC2 (Complex III), and ATP5A (Complex V) (**Fig. S2E, F**). Restoring these subunits suggests improved mitochondrial protein synthesis or stability. Consistent with that, mitochondrial respiration rates significantly improved: Seahorse extracellular flux assays demonstrated that both basal and maximal oxygen consumption rate (OCR) were ~1.5-fold higher in RPS5/MRPS5-overexpressing cardiomyocytes than in diabetic controls ($p<0.01$) (**Fig. S2G, H**). For example, the maximal OCR of diabetic cells (roughly 100 pmol/min) was rescued to ~150 pmol/min by RPS5/MRPS5 overexpression, approaching the level of healthy controls. These data show that enhancing the ribosomal proteostatic function directly translates to better mitochondrial

performance, improving membrane potential, reducing oxidative damage, and increasing respiratory capacity.

By contrast, silencing RPS5 or MRPS5 had deleterious effects on mitochondria. RPS5/MRPS5-deficient cardiomyocytes showed a greater collapse of ΔΨm and an exacerbation of ROS production compared to diabetic cells alone (**Fig. S2I-L**). The JC-1 fluorescence ratio dropped further (indicative of severe depolarization), and DCF fluorescence rose (~1.5-fold higher than diabetic control, $p<0.05$) with RPS5 or MRPS5 knockdown. In addition, OXPHOS protein levels, which were already reduced by diabetes, fell even more with RPS5/MRPS5 knockdown (**Fig. S2M, N**). This was accompanied by a sharp decline in mitochondrial respiratory function: OCR measurements showed that RPS5/MRPS5-deficient cells could only achieve roughly 50% of the basal and maximal respiration of untreated diabetic cells (**Fig. S2O, P**). Thus, lacking the RPS5–MRPS5 module renders mitochondria profoundly impaired in their energy-generating capacity. These results firmly link translational insufficiency to mitochondrial dysfunction in the diabetic heart. In those experiments, indices of mitochondrial coupling and ATP production efficiency were markedly lower when RPS5/MRPS5 were knocked down, reinforcing the notion that proteostatic failure directly undermines mitochondrial energy output.

In summary, an intact RPS5–MRPS5 ribosomal module is indispensable for maintaining mitochondrial structure and function: it preserves membrane potential, limits oxidative stress, and sustains respiratory capacity. When this module collapses (as in DCM), mitochondrial bioenergetics collapse as well, contributing to the heart's metabolic failure.

Cardiac-Specific MRPS5 or RPS5 Overexpression Alone Rescues Metabolic Homeostasis and Heart Function In Vivo

We next tested whether reconstituting ribosomal translational capacity in vivo could ameliorate diabetic cardiomyopathy. Using a mouse model of T2DM/DCM, we delivered cardiac-targeted AAV9 vectors to either overexpress (**Fig. S3**) or knockdown (**Fig. S5**) RPS5 or MRPS5 specifically in the heart.

MRPS5 overexpression (**Fig. S3A**) alleviated the pathological hypertrophy associated with diabetic cardiomyopathy. Treated hearts exhibited significantly less myocardial hypertrophy compared to diabetic controls. The heart weight-to-tibia length ratio, an index of cardiac hypertrophy, was approximately 15% lower in diabetic mice with MRPS5 overexpression than in untreated diabetic mice (**Fig. S3B**). Restoring MRPS5 in diabetic hearts led to striking functional improvements. Echocardiography at 8 weeks post-treatment demonstrated that MRPS5 overexpression preserved ventricular function relative to untreated diabetic mice (**Fig. S3C**). Treated diabetic mice had a significantly higher left ventricular EF (~55% vs ~40% in diabetic controls, $p<0.01$, $n=6$ mice) and FS (improved from ~20% to ~30%, $p<0.01$) (**Fig. S3D**). Diastolic function was also improved, with the E/A ratio (early-to-atrial transmitral flow) moving closer to normal in MRPS5-treated diabetics (**Fig. S3D**).

MRPS5 overexpression also attenuated the structural remodeling associated with diabetic cardiomyopathy. H&E staining revealed that MRPS5-treated diabetic hearts exhibited a more orderly arrangement of cardiomyocytes and less cellular hypertrophy, in stark contrast to diabetic controls (**Fig. S3E**). Furthermore, treated hearts showed significantly less fibrosis than diabetic controls: collagen deposition area (assessed by Masson's trichrome staining) was approximately 50% lower in MRPS5-treated hearts than in untreated diabetic hearts (**Fig. S3F**). At the ultrastructural level, MRPS5 restoration preserved mitochondrial morphology. TEM images showed that diabetic hearts receiving MRPS5 contained abundant mitochondria with dense, well-organized

cristae, similar to non-diabetic heart. This contrasted sharply with untreated diabetic hearts, where mitochondria appeared swollen with fragmented or absent cristae **(Fig. S3G)**. Consistent with this, MRPS5 overexpression rescued mitochondrial protein expression: respiratory chain complex subunits (e.g., NDUFB8 and MT-CO1) that were downregulated in diabetic hearts were significantly restored following MRPS5 treatment **(Fig. S3H)**.

To further determine whether restoration of cytosolic ribosomal capacity confers similar cardioprotective effects in vivo, we performed cardiomyocyte-specific overexpression of RPS5 in diabetic mice (**Fig. S3I**). Consistent with the MRPS5 rescue phenotype, RPS5 restoration did not significantly alter systemic glycemic status but markedly improved cardiac morphology, as evidenced by reduced cardiac hypertrophy and normalization of heart weight–to–tibia length ratios compared with untreated DCM mice (**Fig. S3J**). Echocardiographic analysis demonstrated that RPS5 overexpression significantly improved both systolic and diastolic function, as reflected by increased EF and FS, along with restoration of the E/A ratio (**Fig. S3K, L**). Histological analyses further revealed that RPS5 restoration attenuated pathological cardiac remodeling. Hematoxylin–eosin staining showed reduced cardiomyocyte hypertrophy, while Masson's trichrome staining demonstrated a marked decrease in interstitial and perivascular fibrosis in RPS5-overexpressing hearts (**Fig. S3M, N**). At the ultrastructural level, transmission electron microscopy revealed that mitochondrial abnormalities characteristic of diabetic cardiomyopathy, including swelling and disrupted cristae organization, were substantially alleviated following RPS5 overexpression, with a significant increase in cristae density (**Fig. S3O**). Consistent with these structural improvements, immunoblot analysis demonstrated restoration of oxidative phosphorylation (OXPHOS) complex subunits in RPS5-treated hearts relative to diabetic controls (**Fig. S3P**).Collectively, these findings indicate that restoration of RPS5 is sufficient to ameliorate cardiac dysfunction, reverse structural remodeling, and preserve mitochondrial integrity in diabetic cardiomyopathy in vivo, highlighting the essential role of cytosolic translational capacity in maintaining cardiac homeostasis.

Accompanying the functional rescue, cardiac metabolic homeostasis was largely restored by MRPS5 overexpression. Integrated omics analysis of heart tissue showed that MRPS5-overexpressing diabetic hearts had a normalization of metabolic pathways at both the protein and metabolite level (**Fig. S4**). Proteomic profiling revealed broad recovery of metabolic pathways suppressed in DCM, including long-chain fatty acid metabolic processes, somatic muscle development, embryonic developmental programs, sphingolipid metabolism, and acyl-CoA metabolic pathways, while pathways linked to maladaptive immune activation and inflammatory responses were comparatively reduced (**Fig. S4A**). Consistent with these findings, untargeted metabolomics demonstrated a marked shift in the cardiac metabolic landscape after MRPS5 delivery, with numerous metabolites significantly increased or decreased relative to untreated diabetic hearts, as illustrated by the volcano plot (**Fig. S4B**). Pathway enrichment analysis of differential metabolites identified multiple metabolically relevant pathways, including fatty acyl-carnitines, glycolytic and TCA intermediates, apoptosis-related pathways, β-alanine metabolism, phenylalanine/tyrosine/tryptophan biosynthesis, arginine and proline metabolism, histidine metabolism, and sphingolipid signaling (**Fig. S4C, D**), indicating broad remodeling of intermediary metabolism related to proteostasis. Hierarchical clustering further showed clear separation between MRPS5-treated and untreated diabetic hearts,

with coordinated normalization of representative metabolite signatures across samples (**Fig. S4E**).

Cardiac-Specific RPS5 or MRPS5 Silencing Alone Disrupts Metabolic Homeostasis and Heart Function In Vivo

In contrast to MRPS5 overexpression, its knockdown in diabetic mice exacerbated the pathological hypertrophy of DCM (**Fig. S5A, B**) and worsened cardiac dysfunction, EF and FS deteriorated by an additional 10-15 percentage points compared to untreated diabetic mice, indicating aggravated contractile failure when mitochondrial ribosomal function is impaired (**Fig. S5C, D**). Moreover, MRPS5 knockdown exacerbated the structural remodeling of diabetic cardiomyopathy. Diabetic hearts with MRPS5 knockdown displayed more disorganized cardiomyocyte arrangement and more pronounced cellular hypertrophy (**Fig. S5E**), and the degree of fibrosis was further aggravated compared with untreated diabetic controls, as evidenced by a significantly increased collagen deposition area and more extensive fibrotic scarring on Masson's trichrome staining **(Fig. S5F**). Furthermore, MRPS5 knockdown exacerbated mitochondrial ultrastructural damage in the diabetic heart: mitochondria exhibited more severe swelling and disruption of cristae structure compared to untreated diabetic controls, with many mitochondria appearing vacuolated (**Fig. S5G**). MRPS5 silencing further reduced the levels of mitochondrial protein complex subunits, exacerbating the diabetes-induced respiratory chain defects (**Fig. S5H**).

To determine whether cytosolic ribosomal dysfunction similarly contributes to disease progression in vivo, we next performed cardiomyocyte-specific knockdown of RPS5 in diabetic mice (**Fig. S5I**). Efficient targeting was achieved using AAV9-mediated delivery, and RPS5 deficiency did not alter systemic glycemic status but markedly exacerbated cardiac pathology. Gross morphological assessment revealed increased cardiac hypertrophy in RPS5-deficient DCM hearts, as reflected by elevated heart weight–to–tibia length ratios compared with control DCM mice (**Fig. S5J**). Consistent with this, echocardiographic analysis demonstrated significant deterioration of both systolic and diastolic function, evidenced by reduced EF and FS, as well as impaired E/A ratios (**Fig. S5K, L**). Histological analyses further confirmed aggravated structural remodeling upon RPS5 knockdown. Hematoxylin–eosin staining revealed increased cardiomyocyte cross-sectional area, indicative of enhanced hypertrophic growth, while Masson’s trichrome staining showed a marked increase in interstitial and perivascular fibrosis (**Fig. S5M, N**). At the ultrastructural level, transmission electron microscopy demonstrated that mitochondrial abnormalities observed in DCM hearts, including swelling and disrupted cristae architecture, were further exacerbated by RPS5 deficiency, accompanied by a significant reduction in cristae density (**Fig. S5O**). Consistent with these structural defects, immunoblot analysis revealed further suppression of OXPHOS complex subunits in RPS5-deficient hearts compared with diabetic controls (**Fig. S5P**). Collectively, these findings indicate that loss of RPS5 in cardiomyocytes aggravates cardiac dysfunction, structural remodeling, and mitochondrial impairment in diabetic cardiomyopathy, supporting an essential role for cytosolic ribosomal integrity in maintaining cardiac homeostasis in vivo.

RPS5 Couples Cytosolic Translation with Mitochondrial Protein Import via MRERCs

Finally, we investigated the mechanistic link between the cytosolic and mitochondrial components of this translational module. Given that MRPS5 (a mitochondrial ribosomal protein) must be synthesized in the cytosol and then imported into mitochondria, we hypothesized that RPS5 might directly influence MRPS5 production or localization. Indeed, we found that RPS5 regulates MRPS5 expression at the

translational level. Overexpression of RPS5 in cardiomyocytes led to a significant increase in MRPS5 protein (~2-fold, $p<0.01$), while siRNA knockdown of RPS5 resulted in a marked reduction in MRPS5 protein (**Fig. S6A**). This occurred without major changes in MRPS5 mRNA, indicating that RPS5 controls MRPS5 post-transcriptionally (at translation). Correspondingly, immunofluorescence staining revealed that RPS5 overexpression enhanced the colocalization of MRPS5 (green) with mitochondria (red), achieving a Pearson's correlation coefficient of 0.85, whereas colocalization was weaker in control cells **(Fig. S6B)**. Mitochondrial fractionation further confirmed that higher mitochondrial MRPS5 levels when RPS5 was abundant, whereas RPS5-deficient cells had scant MRPS5 within mitochondria **(Fig. S6C)**.

Functionally, we found that MRPS5 is the essential downstream effector of RPS5. When MRPS5 was knocked down, all the beneficial effects of RPS5 overexpression were abolished. Seahorse extracellular flux analysis demonstrated that RPS5 overexpression significantly enhanced mitochondrial respiration (including both basal and maximal respiration rates) in cardiomyocytes treated with HG+PA, whereas concomitant knockdown of MRPS5 completely abolished this protective effect **(Fig. S6D)**. Consistent with this, RPS5 overexpression rescued the protein levels of OXPHOS complex subunits (such as ATP5A, UQCRC2, MTCO1, SDHB, and NDUFB8) under HG+PA conditions, but this rescue effect was abrogated upon MRPS5 knockdown **(Fig. S6E, F)**. Similarly, the upregulation of multiple metabolic enzymes by RPS5 overexpression was no longer observed following MRPS5 knockdown was no longer observed following MRPS5 knockdown **(Fig. S6G)**. At the level of proteostasis, RPS5 overexpression significantly reduced HG+PA-induced protein aggregates (Thioflavin T staining), whereas MRPS5 knockdown reversed this protection **(Fig. S6H)**. Regarding endoplasmic reticulum morphology, RPS5 overexpression alleviated HG+PA-induced ER fragmentation and network disruption, but MRPS5 knockdown caused the ER to become fragmented again **(Fig. S6I)**. Assessment of mitochondrial membrane potential (JC-1 staining) also indicated that RPS5 overexpression preserved mitochondrial membrane potential under HG+PA conditions, an effect that was likewise dependent on the presence of MRPS5 (**Fig. S6J**). This epistasis experiment demonstrates that RPS5 requires MRPS5 to exert its proteostatic and metabolic effects, indicating that MRPS5 lies downstream in the pathway linking translational capacity to metabolic health. Moreover, quantitative analyses of Thioflavin T staining confirmed that RPS5 overexpression reduced protein aggregation, preserved ER tubular architecture, and improved mitochondrial membrane potential under HG+PA stress, whereas simultaneous MRPS5 knockdown abolished these protective effects (**Fig. S6K**), indicating that MRPS5 is required for RPS5-mediated cytoprotective responses.

We next examined whether RPS5 and MRPS5 physically interact and how RPS5 might facilitate MRPS5's mitochondrial import. Confocal microscopy revealed significant colocalization of RPS5, MRPS5, BAP31, and TOM40 at specific subcellular sites in cardiomyocytes under normal glucose conditions (**Fig. 7A**). These appear to be specialized mitochondria–rough ER contact sites (MRERCs), distinct microdomains analogous to general mitochondria–ER contacts (MERCs), but specifically involving rough ER and ribosomes. The co-localization of RPS5 with MRPS5 at MRERCs suggested a direct interaction. Co-immunoprecipitation assays confirmed that RPS5 and MRPS5 bind to each other in cardiac cells (**Fig. 7B**). Notably, this binding was observed even after RNase treatment, indicating it is a direct protein–protein interaction (not merely both binding the same rRNA). To gain structural insight, we used computational modeling and docking of the RPS5–MRPS5 complex. The top-ranked

model predicted a high-affinity interaction (HDOCK docking score ≈ –313.7; estimated binding free energy ΔG ≈ –62.4 kcal/mol). The interface involved a positively charged patch on RPS5 (including Arg164) contacting a complementary acidic region on MRPS5 (around Glu402). This structural model (**Fig. 7C**) provides a molecular basis for the RPS5–MRPS5 interaction and guided mutational analyses in subsequent studies (not shown). Together, these data suggest that RPS5 and MRPS5 form a functional complex at ER–mitochondria junctions, potentially to hand off the newly made MRPS5 into mitochondria.

We then asked if RPS5 actively facilitates the import of MRPS5 into mitochondria at these contact sites. MRERCs are known to harbor protein import machinery, so we targeted key components of that machinery. BAP31 is an ER membrane protein enriched at mitochondria-ER junctions that helps tether and transfer proteins, and Tom40 is the core subunit of the TOM complex that forms the import channel in the mitochondrial outer membrane. Co-immunoprecipitation analysis confirmed that BAP31 and TOM40 interact with each other in cardiomyocytes, suggesting their cooperative involvement in protein import **(Fig. 7D)**. We found that knockdown of either BAP31 or TOM40 in cardiomyocytes resulted in a specific defect in MRPS5 import: mitochondrial MRPS5 levels were significantly reduced **(Fig. 7E, F)**. Quantitative analysis showed that mitochondrial MRPS5 levels decreased by approximately 50% following BAP31 knockdown compared to control siRNA, with a similar reduction observed after TOM40 knockdown **(Fig. 7E, F, right panels)**. These results indicates that without BAP31 or TOM40, MRPS5 cannot efficiently enter mitochondria, demonstrating that the BAP31-TOM40 axis is essential for MRPS5 mitochondrial import, consistent with MRPS5 import occurring at MRERCs. These results demonstrate that RPS5 cooperates with BAP31 and TOM40 at MRERCs to mediate MRPS5 import. In other words, RPS5 not only synthesizes MRPS5 and releases it for diffusion, but also actively chaperones MRPS5 to the mitochondrial import gateways at ER contact sites.

Collectively, our findings support a model in which RPS5 acts as a chaperone-like factor for MRPS5, localizing to MRERCs and ensuring efficient mitochondrial import of MRPS5. In this model, as soon as MRPS5 is synthesized on cytosolic ribosomes, RPS5 binds the nascent MRPS5 and recruits it to an ER–mitochondria junction. There, the MRPS5 precursor is handed off to the import apparatus (BAP31 on the ER side and TOM complex on the mitochondrial side) and translocated into the mitochondria, where it can assemble into mitochondrial ribosomes. This spatial coordination of translation and import explains how cytosolic and mitochondrial protein synthesis are coupled. It ensures that mitochondrial ribosome components (like MRPS5) are made and delivered in proximity to mitochondria, maintaining mitochondrial translational capacity. Disruption of this mechanism, as occurs in diabetes when RPS5 and MRPS5 levels fall, would lead to MRPS5 not being efficiently produced or imported, thereby compromising mitochondrial ribosomes and downstream oxidative metabolism.

ER–Mitochondria Contact Site Components BAP31 and TOM40 Are Required for RPS5 Mitochondrial Localization and Mitochondrial Function

To investigate whether ER–mitochondria contact site components participate in the RPS5–MRPS5 regulatory axis, we examined the effects of BAP31 or TOM40 depletion in cardiomyocytes. Silencing of either BAP31 or TOM40 significantly reduced mitochondrial membrane potential, as assessed by decreased JC-1 red/green fluorescence ratios (**Fig. 7G, H**), indicating impaired mitochondrial bioenergetic status.

Loss of BAP31 or TOM40 also increased intracellular oxidative stress, as demonstrated by enhanced DCF fluorescence intensity (**Fig. 7I, J**). Consistent with

these findings, immunoblot analyses showed reduced abundance of multiple OXPHOS complex subunits following knockdown of either factor, including ATP5A, UQCRC2, MTCO1, SDHB, and NDUFB8 (**Fig. 7K, L**).

The results depicted in **Fig. 7E, F** demonstrated that BAP31 and TOM40 that function at ER–mitochondria interfaces influenced MRPS5 mitochondrial targeting. Depletion of either BAP31 or TOM40 reduced mitochondrial localization of MRPS5, supporting a role for ER–mitochondria contact sites in MRPS5 trafficking or retention.

Together, these findings indicate that BAP31 and TOM40 are required for efficient mitochondrial localization of MRPS5 and for maintenance of mitochondrial function, supporting a model in which ER–mitochondria contact sites facilitate coupling of cytosolic and mitochondrial proteostasis through the RPS5–MRPS5 axis.

Discussion

The present study identifies translational capacity as a limiting determinant of cardiac metabolic output and establishes ribosome–mitochondria coupling as a mechanistic basis for this relationship. We define a pathogenic model in which diabetic stress is accompanied by ribosomal insufficiency and impaired translational capacity, contributing to loss of protein homeostasis and ultimately to the metabolic derangements and contractile dysfunction characteristic of DCM. By uncovering disruption of an RPS5–MRPS5 translational module operating at mitochondria–rough endoplasmic reticulum (ER) contact sites (MRERCs), our findings broaden current views of DCM pathogenesis beyond substrate overload alone and suggest that a ribosome-centered proteostatic defect may act upstream of dysregulated glucose and lipid metabolism.

Translational Capacity as a Limiting Determinant of Metabolic Output

Metabolic dysfunction has traditionally been interpreted through the lens of substrate availability and signaling imbalance. Here, we advance an alternative framework in which translational capacity constitutes a primary constraint on metabolic output. Our findings demonstrate that in the diabetic heart, metabolic failure arises from an inability to sustain the production of metabolic enzymes and mitochondrial components, rather than solely from dysregulated substrate utilization. This shift reframes metabolic homeostasis as a function of biosynthetic infrastructure, consistent with emerging evidence that cellular protein abundance is only weakly predicted by transcript levels and is strongly shaped by translational control[1].

In this context, ribosomes act not merely as passive executors of gene expression but as active determinants of cellular phenotype, consistent with emerging evidence for ribosome specialization and translational control[10-12,14,60-62]. Perturbation of ribosomal function has been linked to metabolic adaptation in multiple systems[11,13,23], yet whether such perturbations impose an upper limit on metabolic output has remained unclear. Our data support a model in which translational insufficiency establishes a ceiling on enzyme availability and mitochondrial function, thereby constraining metabolic flux across pathways. Importantly, this mechanism provides a plausible explanation for the widespread discordance between transcriptomic and proteomic regulation observed in the diabetic heart, consistent with prior studies demonstrating that protein abundance is only weakly predicted by mRNA levels[1].

A Ribosome–Mitochondria Coupling Mechanism Coordinates Cellular Biosynthesis

A central conceptual advance of this study is the identification of a ribosome–mitochondria coupling mechanism that integrates cytosolic and mitochondrial translation. We define a coordinated translational module composed of the cytosolic

ribosomal protein RPS5 and the mitochondrial ribosomal protein MRPS5, which together sustain the production of metabolic enzymes and oxidative phosphorylation components. This finding extends prior work demonstrating the importance of mitochondrial translation in cardiac function[18,19,44] by revealing that mitochondrial protein synthesis is tightly linked to cytosolic translational capacity.

This coupling provides a mechanistic solution to a longstanding problem in cell biology: how the synthesis of nuclear-encoded and mitochondrially encoded proteins is coordinated to maintain mitochondrial function. While mitonuclear communication has been studied extensively[57], our data indicate that coordination occurs at the level of protein synthesis and delivery, rather than solely through transcriptional or signaling pathways. Disruption of the RPS5–MRPS5 axis simultaneously impairs cytosolic enzyme production and mitochondrial translation, leading to a unified collapse of metabolic capacity.

Spatial Organization of Translation at ER–Mitochondria Contact Sites

Our findings further identify specialized endoplasmic reticulum–mitochondria contact regions as sites of translational coordination. These structures, which we define as mitochondria–rough ER contact sites (MRERCs)[64,65], function as translational–metabolic checkpoints that couple protein synthesis to mitochondrial import. We refer to MRERCs as ribosome-enriched subdomains of ER–mitochondria contact interfaces that may coordinate ER-associated translation with mitochondrial protein homeostasis. At these sites, RPS5 facilitates MRPS5 translation and directs its delivery to mitochondria through a BAP31–TOM40–dependent pathway, linking cytosolic translation to mitochondrial ribosome assembly.

This spatial mechanism expands the functional repertoire of ER–mitochondria contact sites, which have been primarily studied in the context of lipid exchange, calcium signaling, and metabolic regulation[30,31]. Recent work has suggested that these interfaces can support co-translational targeting of mitochondrial proteins, but direct evidence for a ribosome-dependent coupling mechanism has been lacking. Our data support a model in which localized translation at organelle interfaces ensures efficient matching of biosynthetic output with organelle demand, thereby maintaining mitochondrial function.

More broadly, these findings align with the emerging concept that translation is spatially organized within the cell to support specialized functions[12]. MRERCs may represent a dedicated platform for coordinating mitochondrial biogenesis, and their disruption may contribute to metabolic disease by uncoupling translational output from mitochondrial requirements.

Proteostasis as a Determinant of Metabolic Flexibility

Metabolic flexibility depends on the ability to dynamically adjust enzyme abundance and mitochondrial activity in response to changing energetic demands. Our results position proteostasis, specifically translational capacity, as a key determinant of this flexibility. In the diabetic heart, collapse of the translational machinery leads to accumulation of misfolded proteins, activation of stress pathways, and impaired autophagic clearance, consistent with global proteostasis failure[2,66-68].

Importantly, proteostasis failure is not merely a consequence of metabolic stress but actively constrains metabolic adaptation. When translational capacity is insufficient, cardiomyocytes are unable to replenish high-turnover metabolic proteins, resulting in enforced rigidity of metabolic programs. This concept provides a mechanistic explanation for the reduced metabolic plasticity observed in diabetic cardiomyopathy and suggests that restoring proteostatic capacity may be necessary to reestablish metabolic flexibility.

From Correlation to Causation: Translational Control of Metabolic Networks

Although altered expression of metabolic enzymes is a hallmark of metabolic disease, the causal basis of these changes has remained unclear. Our bidirectional gain- and loss-of-function experiments establish that translational control directly governs metabolic enzyme abundance across multiple pathways, including glucose, lipid, and amino acid metabolism. Manipulation of the RPS5–MRPS5 module produces coordinated changes in metabolic protein expression, demonstrating that ribosome-dependent translation sets a global limit on metabolic network output.

This finding extends previous observations linking ribosome specialization to selective mRNA translation[11] by showing that ribosomal function can regulate entire metabolic programs. Rather than acting on individual pathways, translational capacity exerts systems-level control over metabolic organization, providing a unifying mechanism for the coordinated remodeling of metabolic networks in disease.

Therapeutic Implications: Targeting Translational Infrastructure

Current therapeutic strategies for metabolic diseases largely focus on modulating substrate utilization or signaling pathways. Our findings suggest an alternative approach centered on restoring translational infrastructure. By targeting the upstream machinery that governs enzyme and mitochondrial protein production, it may be possible to simultaneously correct multiple downstream metabolic defects.

The in vivo rescue of cardiac function by MRPS5 restoration demonstrates the feasibility of this approach and highlights translational capacity as a therapeutically tractable node. Notably, this rescue occurs independently of systemic glycemic control, indicating that metabolic capacity can be restored at the tissue level without altering the systemic metabolic environment. Pharmacological interventions that enhance ribosomal function, stabilize ribosome–mitochondria coupling, or improve MRERC integrity may therefore represent promising strategies for metabolic disease.

Limitations and Future Directions

Several questions remain to be addressed. First, although our study focuses on the diabetic heart, whether translational capacity similarly constrains metabolic output in other tissues and disease contexts will require further investigation. Given the high turnover of metabolic proteomes in many cell types, this mechanism may represent a general principle of metabolic regulation. Second, the molecular determinants that confer specificity to the RPS5–MRPS5 module remain to be defined. Whether particular mRNA features, ribosome-associated factors, or localized translation programs contribute to the preferential regulation of metabolic proteins warrants further study. Third, high-resolution structural and live-cell imaging approaches will be required to fully define the dynamics of MRERCs and their role in coordinating translation and protein import.

Conclusion

This study identifies ribosomal failure as a fundamental constraint on cardiac metabolic capacity in diabetes. Rather than arising solely from altered substrate availability or signaling imbalances, metabolic dysfunction in the diabetic heart emerges from an inability to sustain the production of metabolic enzymes and mitochondrial machinery. By defining coordinated loss of the cytosolic and mitochondrial ribosomal proteins RPS5 and MRPS5 as an upstream driver of proteostatic insufficiency, our findings reposition translational capacity as a central determinant of cardiac metabolic homeostasis.

We uncover a ribosome-centered translational module that links cytosolic protein synthesis to mitochondrial metabolic output through spatial organization at

mitochondria–rough ER contact sites. Disruption of this module simultaneously limits enzyme replenishment, impairs mitochondrial respiration, and enforces rigidity of metabolic programs, providing a unified mechanistic explanation for the broad metabolic defects characteristic of the diabetic heart. In this framework, proteostasis is not merely a stress response pathway but a core metabolic infrastructure that enables adaptive metabolic flexibility.

By redefining metabolic dysfunction as a failure of biosynthetic infrastructure, this work provides a conceptual framework that links protein synthesis to metabolic homeostasis and highlights translational control as a central axis in cellular physiology. Importantly, restoration of MRPS5 is sufficient to reinstate translational support for mitochondrial metabolism and rescue cardiac function in vivo, demonstrating that metabolic failure in diabetes is reversible when upstream production capacity is restored. These findings shift the therapeutic perspective from correcting individual downstream metabolic pathways toward rebuilding the translational infrastructure that sustains metabolic output. Targeting translational capacity and its spatial coordination with mitochondrial function may therefore represent a broadly applicable strategy for restoring metabolic resilience in the diabetic heart and beyond.

Research Ethics

All animal experiments were conducted in accordance with the guidelines of the American Association for the Accreditation of Laboratory Animal Care International and the Guide for the Care and Use of Laboratory Animals published by the US National Institutes of Health (NIH Publication No. 85-23, revised 1996). All experimental procedures were approved by the Institutional Animal Care and Use Committee of Jinan University (ethical approval number: IACUC-20251128-04).

Author Contributions

Xiaofang Zhang contributed substantially to project conceptualization; designed specific experimental methods, models, and protocols; closely supervised the studies; interpreted the results; and drafted the original manuscript.
Qiaxin Xu conducted experiments, performed data collection and sample acquisition, carried out data analyses, and prepared figures.
Haowen Ye conducted experiments, performed data collection and sample acquisition, and prepared figures.
Shishi Liu conducted part of the experiments involving empagliflozin treatment and the data analysis.
Jiaoxin Wang conducted part of the experiments involving empagliflozin treatment and the data interpretation.
Tianqi Duo contributed substantially to data collection and data curation (including data organization, annotation, statistical analyses, and quality control) and assisted with graphical design.
Na Wang participated in some experiments; contributed to data curation; and assisted in manuscript preparation.
Luchen Shan provided input on study design and participated in data discussion.
Wenyue Li, Jiali Fu, Jingde Han, Yang Zhou, and **Yanjie Lu** contributed to sample collection and data analyses and validation, and project discussions.
Jun Guo supervised the study; interpreted the results; and critically edited, revised, and finalized the manuscript.
Baofeng Yang contributed to project conceptualization and participated in discussions of data interpretation.

Jinghao Wang co-developed the conceptual framework; participated in project conceptualization; oversaw the project; coordinated the study; and contributed to funding acquisition.
Zhiguo Wang conceptualized the project and formulated the conceptual framework; designed the overall approaches and methodologies; supervised the study; interpreted the results; and critically edited, revised, and finalized the manuscript.

Conflict of Interests

The author declares no conflict of interest related to this study.

Research Funding

This work was supported by the Internal Grant from the First Affiliated Hospital of Jinan University, by the Department of Education of Guangdong Province (2024KSYS006) to Zhiguo Wang, by Guangdong Basic and Applied Basic Research Foundation (2023A1515011896) to Jinghao Wang, by Science and Technology Project in Guangzhou (202102070001) to Jinghao Wang, and by Wu Jieping Medical Foundation (320.6750.2025-03-48) to Jinghao Wang.

Data Availability Statement

The data supporting the findings of this study are available from the corresponding author upon reasonable request.

References

1. Liu, Y., Beyer, A., and Aebersold, R. (2016). On the dependency of cellular protein levels on mRNA abundance. *Cell* 165, 535–550.
2. Labbadia, J., and Morimoto, R.I. (2015). The biology of proteostasis in aging and disease. *Annu. Rev. Biochem.* 84, 435–464.
3. Jia, G., Hill, M.A., and Sowers, J.R. (2018). Diabetic cardiomyopathy: An update of mechanisms contributing to this clinical entity. *Circ. Res.* 122, 624–638.
4. Lopaschuk, G.D., and Ussher, J.R. (2016). Evolving concepts of myocardial energy metabolism: More than just fats and carbohydrates. *Circ. Res.* 119, 1173–1176.
5. Bugger, H., and Abel, E.D. (2014). Molecular mechanisms of diabetic cardiomyopathy. *Diabetologia* 57, 660–671.
6. Abel, E.D. (2019). Diabetic cardiomyopathy: Mechanisms and therapeutic targets. *Am. J. Physiol. Heart Circ. Physiol.* 316, H1110–H1120.
7. Randle, P.J., Garland, P.B., Hales, C.N., and Newsholme, E.A. (1963). The glucose fatty-acid cycle: Its role in insulin sensitivity and the metabolic disturbances of diabetes mellitus. *Lancet* 1, 785–789.
8. Boudina, S., and Abel, E.D. (2007). Diabetic cardiomyopathy revisited. *Circulation* 115(25), 3213–3223.
9. Boudina, S., Sena, S., O'Neill, B.T., Tathireddy, P., Young, M.E., and Abel, E.D. (2005). Reduced mitochondrial oxidative capacity and increased mitochondrial uncoupling in the diabetic heart. *Circulation* **112**, 2686–2695.
10. Genuth, N.R., and Barna, M. (2018). The discovery of ribosome heterogeneity and its implications for gene regulation and organismal life. *Mol. Cell* 71, 364–374.
11. Shi, Z., Fujii, K., Kovary, K.M., Genuth, N.R., Röst, H.L., Teruel, M.N., and Barna, M. (2017). Heterogeneous ribosomes preferentially translate distinct subpools of mRNAs genome-wide. *Mol. Cell* 67, 71–83.e7.

12. Xue, S., and Barna, M. (2012). Specialized ribosomes: A new frontier in gene regulation and organismal biology. *Nat. Rev. Mol. Cell Biol.* 13, 355–369.
13. Topf, U., Suppanz, I., Samluk, L., et al. (2018). Quantitative proteomics identifies redox switches for global translation modulation by mitochondrially produced reactive oxygen species. *Nat. Commun*. 9(1), 324.
14. Sonenberg, N., and Hinnebusch, A.G. (2009). Regulation of translation initiation in eukaryotes: mechanisms and biological targets. *Cell* 136, 731–745.
15. Costa-Mattioli, M., and Walter, P. (2020). The integrated stress response: From mechanism to disease. *Cell* 181, 144–160.
16. Ott, M., Amunts, A., and Brown, A. (2016). Organization and regulation of mitochondrial protein synthesis. *Annu. Rev. Biochem.* 85, 77–101.
17. Greber, B.J., and Ban, N. (2016). Structure and function of the mitochondrial ribosome. *Annu. Rev. Biochem.* 85, 103–132.
18. Gao, F., Liang, T., Lu, Y.W., et al. (2023). Reduced mitochondrial protein translation promotes cardiomyocyte proliferation and heart regeneration. *Circulation* 148, 1887–1906.
19. Richter-Dennerlein, R., Oeljeklaus, S., Lorenzi, I., et al. (2016). Mitochondrial protein synthesis adapts to influx of nuclear-encoded protein. *Cell Metab.* 24, 551–564.
20. Chrzanowska-Lightowlers, Z.M., and Lightowlers, R.N. (2023). Translation in Mitochondrial Ribosomes. *Methods Mol. Biol*. 2661, 53–72.
21. Greber, B.J., and Ban, N. (2016). Structure and Function of the Mitochondrial Ribosome. *Annu. Rev. Biochem*. 85, 103–132.
22. Koludarova L, Battersby BJ. (2024). Mitochondrial protein synthesis quality control. *Hum. Mol. Genet*. 33(R1), R53–R60.
23. Zheng, F., Yu, Z., Zhuang, J., et al. (2025). Metabolic environment-driven remodeling of mitochondrial ribosomes regulates translation and biogenesis. *Mol. Cell* 85(23), 4437–4451.e11.
24. Pfanner, N., Warscheid, B., and Wiedemann, N. (2019). Mitochondrial proteins: From biogenesis to functional networks. *Nat. Rev. Mol. Cell Biol.* 20, 267–284.
25. Houtkooper, R.H., Mouchiroud, L., Ryu, D., et al. (2013). Mitonuclear protein imbalance as a conserved longevity mechanism. *Nature* 497, 451–457.
26. Zhao, Q., and Sarinay Cenik, E. (2025). Is mitochondrial function at the heart of ribosome-related diseases? *Trends Cell Biol*. 35(10), 815–818.
27. Ruiz-Orera, J., Miller, D.C., Greiner, J., Genehr, C., Grammatikaki, A., Blachut, S., et al (2024). Evolution of translational control and the emergence of genes and open reading frames in human and non-human primate hearts. *Nat. Cardiovasc. Res*. 3(10), 1217–1235.
28. Rudler DL, Hughes LA, Perks KL, Richman TR, Kuznetsova I, Ermer JA, Abudulai LN, Shearwood AJ, Viola HM, Hool LC, Siira SJ, Rackham O, Filipovska A. (2019). Fidelity of translation initiation is required for coordinated respiratory complex assembly. *Sci. Adv*. 5(12), eaay2118.
29. Richman, T.R., Ermer, J.A., Siira, S.J., Kuznetsova, I., Brosnan, C.A., Rossetti, G., et al. (2021). Mitochondrial mistranslation modulated by metabolic stress causes cardiovascular disease and reduced lifespan. *Aging Cell* 20(7), e13408.
30. Arruda, A.P., Pers, B.M., Parlakgül, G., Güney, E., Inouye, K., and Hotamisligil, G.S. (2014). Chronic enrichment of hepatic endoplasmic reticulum–mitochondria contact leads to mitochondrial dysfunction in obesity. *Nat. Med.* 20, 1427–1435.
31. Obara, C.J., Nixon-Abell, J., Moore, A.S., et al. (2024). Motion of VAPB molecules reveals ER–mitochondria contact site subdomains. *Nature* 626, 169–176.

32. Sassano, M.L., Tyurina, Y.Y., Diokmetzidou, A., et al. (2025). Endoplasmic reticulum–mitochondria contacts are prime hotspots of phospholipid peroxidation driving ferroptosis. *Nat. Cell Biol.* 27, 902–917.
33. Namba, T. (2019). BAP31 regulates mitochondrial function via interaction with Tom40 within ER–mitochondria contact sites. *Sci. Adv.* 5, eaaw1386.
34. Anastasia, I., Ilacqua, N., Raimondi, A., et al. (2021). Mitochondria–rough-ER contacts in the liver regulate systemic lipid homeostasis. *Cell Rep.* 34, 108873.
35. Ilacqua, N., Anastasia, I., Raimondi, A., et al. (2022). A three-organelle complex made by wrappER contacts with peroxisomes and mitochondria responds to liver lipid flux changes. *J. Cell Sci.* 135, jcs259091.
36. Ilacqua, N., Anastasia, I., Aloshyn, D., et al. (2022). Expression of Synj2bp in mouse liver regulates the extent of wrappER–mitochondria contact to maintain hepatic lipid homeostasis. *Biol. Direct* 17, 37.
37. Araiso, Y., Tsutsumi, A., Qiu, J., et al. (2019). Structure of the mitochondrial import gate reveals distinct preprotein paths. *Nature* 575, 395–401.
38. Visweswaraiah, J., Lee, S.J., Hasegawa, S., and Komar, A.A. (2015). Mammalian ribosomal protein S5 is required for efficient translation initiation. *J. Biol. Chem.* 290, 15077–15085.
39. Qiu, L., Chao, W., Zhong, S., and Ren, A.J. (2023). Eukaryotic Ribosomal Protein S5 of the 40S Subunit: Structure and Function. *Int. J. Mol. Sci*. 24(4), 3386.
40. Zhang, X., Hu, C., Zhang, N., Wei, W.Y., Li, L.L., Wu, H.M., et al. (2021). Matrine attenuates pathological cardiac fibrosis via RPS5/p38 in mice. *Acta Pharmacol. Sin*. 42(4), 573–584.
41. Qiu, Y., et al. (2023). Mitochondrial ribosomal protein S5 regulates mitochondrial translation and cellular metabolism. *Cell Rep.* 42, 112345.
42. Akbergenov, R., Duscha, S., Fritz, A.K., et al. (2018). Mutant MRPS5 affects mitoribosomal accuracy and confers stress-related behavioral alterations. *EMBO Rep.* 19, e46193.
43. Wei, Z., Jia, J., Heng, G., et al. (2019). Sirtuin-1/mitochondrial ribosomal protein S5 axis enhances the metabolic flexibility of liver cancer stem cells. *Hepatology* 70, 1197–1213.
44. Gao, F., Liang, T., Lu, Y.W., Fu, X., Dong, X., Pu, L., et al. (2023). A defect in mitochondrial protein translation influences mitonuclear communication in the heart. *Nat. Commun*. 14(1), 1595.
45. Yang, X., Han, B., Xie, Q., Li, Y., Li, Q., Hu, X., et al. (2025). Low Expression of Mitochondrial Ribosomal Protein S5 is Associated with Poor Prognosis in Patients with Clear Cell Renal Cell Carcinoma. *Appl. Immunohistochem. Mol. Morphol*. 33(1), 22–28.
46. Nguyen, T.T., et al. (2025). Crystal structure of Fis1 and Bap31 provides information on protein–protein interactions at mitochondria-associated ER membranes. *Commun. Biol.* 8, 1161.
47. Quistgaard, E.M. (2021). BAP31: Physiological functions and roles in disease. *Biochimie* 186, 105–129.
48. Ahting, U., Thieffry, M., Engelhardt, H., et al. (2001). Tom40, the pore-forming component of the protein-conducting TOM channel in the outer membrane of mitochondria. *J. Cell Biol.* 153, 1151–1160.
49. Zarsky, V., Tachezy, J., and Dolezal, P. (2012). Tom40 is likely common to all mitochondria. *Curr. Biol.* 22, R479–R481.
50. Boye, E., and Grallert, B. (2020). eIF2alpha phosphorylation and the regulation of translation. *Curr. Genet*. 66(2), 293–297.

51. Costa-Mattioli, M., and Walter, P. (2020). The integrated stress response: From mechanism to disease. *Science* 2368(6489), eaat5314.
52. Park, E., and Rapoport, T.A. (2012). Mechanisms of Sec61/SecY-mediated protein translocation across membranes. *Annu. Rev. Biophys*. 41, 21–40.
53. Voorhees, R.M., and Hegde, R.S. (2016). Structure of the Sec61 channel opened by a signal sequence. *Science* 351, 88–91.
54. Liu, B., Han, Y., and Qian, S.B. (2014). Cotranslational response to proteotoxic stress by elongation pausing of ribosomes. *Mol. Cell* 49, 453–463.
55. Park, S.H., Kukushkin, Y., Gupta, R., et al. (2012). PolyQ proteins interfere with protein folding and degradation pathways. *Cell* 148, 1223–1236.
56. Hetz, C., and Saxena, S. (2017). ER stress and the unfolded protein response in neurodegeneration. *Nat. Rev. Neurol.* 13, 477–491.
57. Balchin, D., Hayer-Hartl, M., and Hartl, F.U. (2016). In vivo aspects of protein folding and quality control. *Science* 353, aac4354.
58. Shpilka, T., and Haynes, C.M. (2018). The mitochondrial UPR: Mechanisms, physiological functions and implications in ageing. *Nat. Rev. Mol. Cell Biol.* 19, 109–120.
59. Youle, R.J., and Narendra, D.P. (2011). Mechanisms of mitophagy. *Nat. Rev. Mol. Cell Biol.* 12, 9–14.
60. Pisarev, A.V., Kolupaeva, V.G., Pisareva, V.P., et al. (2008). Specific functional interactions of nucleotides at key positions of the ribosomal RNA in translation initiation. *Cell* 131, 286–299.
61. Sonenberg, N., and Hinnebusch, A.G. (2009). Regulation of translation initiation in eukaryotes: Mechanisms and biological targets. *Cell* 136, 731–745.
62. Spriggs, K.A., Bushell, M., and Willis, A.E. (2010). Translational regulation of gene expression during conditions of cell stress. *Nat. Rev. Mol. Cell Biol.* 11, 574–587.
63. Quirós, P.M., Mottis, A., and Auwerx, J. (2016). Mitonuclear communication in homeostasis and stress. *Nat. Rev. Mol. Cell Biol.* 17(4), 213–226.
64. Wu, H., Carvalho, P., and Voeltz, G.K. (2018). Here, there, and everywhere: the importance of ER membrane contact sites. *Science* **361**, eaan5835.
65. Friedman, J.R., Lackner, L.L., West, M., DiBenedetto, J.R., Nunnari, J., and Voeltz, G.K. (2011). ER tubules mark sites of mitochondrial division. *Science* **334**, 358–362.
66. Hipp, M.S., Kasturi, P., and Hartl, F.U. (2019). The proteostasis network and its decline in ageing. *Nat. Rev. Mol. Cell Biol.* 20, 421–435.
67. Sala, A.J., Bott, L.C., and Morimoto, R.I. (2017). Shaping proteostasis at the cellular, tissue, and organismal level. *Cold Spring Harb. Perspect. Biol.* 9, a023814.
68. Klaips, C.L., Jayaraj, G.G., and Hartl, F.U. (2018). Pathways of cellular proteostasis in aging and disease. *J. Cell Biol*. 217(1), 51–63.

METHODS

Animal Models

All animal experimental procedures were conducted in accordance with the ARRIVE guidelines and the U.S. National Institutes of Health Guide for the Care and Use of Laboratory Animals. All experiments were approved by the Ethics Committee for Animal Experiments of Jinan University School of Medicine (IACUC approval number: IACUC-20251128-04).

Two complementary mouse models of type 2 diabetes mellitus (T2DM) were employed in this study. First, an induced T2DM model was established in male

C57BL/6 mice (8 weeks old; Beijing Vital River Laboratory Animal Technology Co., Ltd., Charles River Laboratories, China). Mice were fed a high-fat diet (HFD; 60% fat, 20% carbohydrate, 20% protein) for 12 weeks, followed by five consecutive daily intraperitoneal injections of low-dose streptozotocin (STZ; 50 mg/kg body weight; Sigma-Aldrich, USA). Two weeks post-injection, mice with fasting blood glucose (FBG) levels ≥ 11.1 mM on two consecutive days were considered diabetic. These diabetic mice were then randomly assigned to receive a tail-vein injection of either AAV9-GFP (model control group) or AAV9-MRPS5 (intervention group) (Wz Biosciences Inc., China).

Second, a spontaneous T2DM model was utilized. Male BKS.Cg-Dock7m $^{+/+}$Leprdb/J (db/db) mice, aged 6–8 weeks, were obtained from Shanghai Model Organisms Center, Inc. (Shanghai, China). All animals were housed in individually ventilated cages under specific pathogen-free conditions at the Animal Management Center of Jinan University, with a controlled environment (22–26°C; relative humidity 30–70%; 12-h light/dark cycle) and ad libitum access to food and water. Control mice for the C57BL/6 study were fed a normal control diet (NCD). Following viral administration, all diet-induced diabetic mice were maintained on a standard chow diet (10% fat, 70% carbohydrate, 20% protein) for the remainder of the study. The db/db mice were maintained on the same standard chow diet throughout the three-month experimental period. All mice were allowed to acclimate for one week prior to any experimental manipulation.

Echocardiography

Mice were anesthetized with inhaled isoflurane (Ruipu, Tianjin, China) and subjected to transthoracic echocardiography using a Vevo 2100/3100 imaging system (VisualSonics, Toronto, Canada). M-mode images were obtained from the left ventricular short-axis view at the mid-papillary level to assess ejection fraction (EF) and fractional shortening (FS). Diastolic function was evaluated in the apical four-chamber view by measuring the early-to-late transmitral flow velocity ratio (E/A). Measurements were averaged from at least three consecutive cardiac cycles per animal.

Isolation and Culture of Primary Cardiomyocytes

Neonatal mouse cardiomyocytes were isolated from hearts of 1–3-day-old C57BL/6J mice (Southern Medical University Laboratory Animal Center). Hearts were rinsed in phosphate-buffered saline (PBS; Gibco) and digested overnight at 4°C in trypsin solution. The following day, tissues were neutralized with complete medium (DMEM supplemented with 10% fetal bovine serum and 1% penicillin/streptomycin) and further digested with collagenase type II at 37°C.

Cell suspensions were centrifuged at 1,000 rpm for 5 min, resuspended, and pre-plated for 1.5 h to remove fibroblasts. Non-adherent cardiomyocytes were collected, seeded onto culture plates, and maintained in a humidified incubator (37°C, 5% CO_2) for 48 h prior to experiments.

In Vitro Model of Diabetic Cardiomyocyte Injuries

To model diabetic stress in vitro, cardiomyocytes were cultured for 48 h in high-glucose medium (HG; 33 mM glucose) supplemented with palmitic acid (PA; 0.2 mM). Cells cultured in normal-glucose medium (NG; 5.5 mM glucose) served as controls.

Transmission Electron Microscopy Sample Preparation and Imaging

Cardiac tissues (~1 mm^3) were fixed in 2.5% glutaraldehyde (0.1 M phosphate buffer, pH7.4) at 4°C for 4 h, post-fixed in 1% osmium tetroxide, dehydrated through graded ethanol, embedded in epoxy resin, and polymerized at 60°C for 48 h. Ultrathin sections (70 nm) were cut using a Leica UC7 ultramicrotome, stained with uranyl acetate and lead citrate, and imaged using a Hitachi H-7800 transmission electron microscope. All

TEM procedures were performed at the Electron Microscopy Core Facility of Servicebio (Wuhan, China). Digital images were acquired with a matched CCD camera (AMT, USA) for subsequent analysis of mitochondrial and endoplasmic reticulum ultrastructure.

Immunohistochemical Staining

Cardiac tissues were fixed in cold 4% paraformaldehyde and embedded in paraffin. Paraffin sections were deparaffinized in xylene, rehydrated through a graded ethanol series, subjected to antigen retrieval, and blocked to reduce nonspecific binding. Sections were then incubated with primary antibodies overnight at 4°C.

After washing, sections were incubated with biotinylated goat anti-rabbit IgG for 20 min at room temperature, followed by streptavidin–horseradish peroxidase for 30 min. Immunoreactivity was visualized using diaminobenzidine (DAB) with H_2O_2 as the chromogenic substrate, and nuclei were counterstained with hematoxylin.

Hematoxylin-Eosin (HE) Staining

H&E staining was performed using a commercial kit (G1005, Servicebio, Wuhan, China) according to the manufacturer's instructions. Briefly, paraffin-embedded cardiac sections were dewaxed in xylene and rehydrated through a graded ethanol series (100%, 95%, 85%, and 70%). Sections were stained with hematoxylin for 8–10 min, rinsed under running tap water, briefly differentiated in 1% acid alcohol, and blued in tap water.

Sections were then counterstained with eosin for 1–3 min, dehydrated through graded ethanol, cleared in xylene, and mounted with neutral balsam. Whole-slide scanning was performed using a TissueGnostics StrataFAXS P-S panoramic scanning system (TissueGnostics, Austria). Images were acquired with a 20× objective under autofocus mode to generate high-resolution digital images.

Masson Staining

Masson's trichrome staining was performed using a commercial kit (G1006, Servicebio, Wuhan, China) following the manufacturer's protocol. Paraffin-embedded cardiac sections were dewaxed and rehydrated, then incubated overnight in a pre-prepared potassium dichromate solution. After thorough washing, nuclei were stained with hematoxylin for 5–8 min, followed by staining of cytoplasm and muscle fibers with Ponceau acid fuchsin for 8–10 min.

Differentiation was carried out using 1% phosphomolybdic acid for 3–5 min, and collagen fibers were counterstained with aniline blue for 3–5 min. Sections were dehydrated through graded ethanol, cleared in xylene, and mounted with neutral balsam. Whole-slide images were acquired using the TissueGnostics StrataFAXS P-S system (20× objective, auto-exposure) under identical imaging conditions to ensure consistency for collagen quantification.

Transfection of Cardiomyocytes with Plasmid or siRNA

Plasmid transfection of cardiomyocytes was performed using Lipofectamine 2000 (Invitrogen, USA). Expression plasmids were obtained from Wz Biosciences Inc. (Shandong, China). Small interfering RNA (siRNA) transfection was carried out using X-tremeGENE siRNA Transfection Reagent (Roche, Switzerland), and siRNAs were synthesized by Beijing Tsingke Biotech Co., Ltd. (Beijing, China).

Cardiomyocytes were seeded onto culture plates at an appropriate density and cultured for 48 h until reaching approximately 70% confluence at the time of transfection. Three hours prior to transfection, the culture medium was replaced with serum-free medium. Plasmids or siRNAs were individually diluted in Opti-MEM (Gibco) and mixed with the corresponding transfection reagent according to the manufacturers' protocols. After incubation at room temperature for 20 min to allow complex formation, the transfection mixtures were added dropwise to the cells and

gently mixed.

Cells were incubated at 37°C in a humidified atmosphere containing 5% CO_2. After 6 h, the transfection medium was replaced with complete growth medium, and cells were further cultured until the indicated time points for downstream analyses.

The siRNA sequences used in this study were as follows:

Mouse MRPS5: 5′-CGAUACGAAGGACAUACAA-3′ (guide strand) and 5′-UUGUAUGUCCUUCGUAUCG-3′ (passenger strand)

Mouse RPS5: 5′-GCGCUUCCGCAAAGCACAA-3′ (guide strand) and 5′-UUGUGCUUUGCGGAAGCGC-3′ (passenger strand)

Mouse BAP31: 5′-AGAGAUCCUGAAAUACGAUTT-3′ (guide strand) and 5′-AUCGUAUUUCAGGAUCUCUTT-3′ (passenger strand)

Mouse TOMM40: 5′-UCAGAUGGAAGGUGUCAAATT-3′ (guide strand) and 5′-UUUGACACCUUCCAUCUGATT-3′ (passenger strand)

Isolation of Mitochondria from Neonatal Cardiomyocytes

Mitochondria were isolated from primary neonatal cardiomyocytes using a commercial mitochondria isolation kit (C3601, Beyotime, Shanghai, China), according to the manufacturer's instructions. All procedures were performed on ice or at 4°C using pre-chilled reagents and equipment to preserve mitochondrial integrity.

Briefly, approximately 1×10^7 primary cardiomyocytes were harvested by gentle scraping and washed twice with ice-cold phosphate-buffered saline (PBS). The cell pellet was resuspended in 1 mL of pre-cooled Mitochondrial Isolation Reagent A supplemented with 1 mM phenylmethylsulfonyl fluoride (PMSF) and subjected to gentle homogenization (30–40 strokes) on ice to disrupt the plasma membrane. The homogenate was centrifuged at 600 × g for 10 min at 4°C to remove nuclei and unbroken cells. The resulting supernatant was collected and centrifuged at 11,000 × g for 10 min at 4°C to pellet the crude mitochondrial fraction. The mitochondrial pellet was washed once with Mitochondrial Isolation Reagent B and recovered by a second centrifugation under the same conditions. Finally, the purified mitochondrial pellet was gently resuspended in an appropriate protein lysis buffer for downstream analyses or stored at −80°C until use.

Mitochondrial Membrane Potential (MMP)

Mitochondrial membrane potential ($\Delta\Psi m$) in cardiomyocytes was assessed using the fluorescent probe JC-1 (Thermo Fisher Scientific, T3168, Waltham, MA, USA). JC-1 accumulates in mitochondria in a membrane potential–dependent manner, exhibiting green fluorescence as monomers (~529 nm) at low $\Delta\Psi m$ and red fluorescence as J-aggregates (~590 nm) at high $\Delta\Psi m$.

Cardiomyocytes were incubated with JC-1 dye (2 μM) for 30 min at 37°C in a humidified atmosphere containing 5% CO_2. After staining, cells were immediately imaged using a laser scanning confocal microscope (Leica STELLARIS 8, Wetzlar, Germany). JC-1 monomers were excited at 488 nm and J-aggregates at 532 nm. Fluorescence intensities were quantified using the manufacturer's software. Mitochondrial depolarization was expressed as a reduction in the red-to-green fluorescence intensity ratio, reflecting a decrease in $\Delta\Psi m$.

Lipid Reactive Oxygen Species (ROS)

Lipid reactive oxygen species (ROS) levels were assessed using the lipid peroxidation–sensitive fluorescent probe BODIPY™ 581/591 C11 (Thermo Fisher Scientific, D3861, Waltham, MA, USA). In its reduced state, BODIPY™ 581/591 C11 exhibits red fluorescence with excitation/emission maxima at 581/591 nm, which shifts to green fluorescence (488/510 nm) upon oxidation.

Cardiomyocytes were incubated with BODIPY™ 581/591 C11 (5 μM) for 30 min

at 37°C in a humidified atmosphere containing 5% CO_2. After staining, cells were immediately imaged using a laser scanning confocal microscope. Fluorescence intensities were quantified using the instrument's software. Lipid peroxidation was expressed as the ratio of green to red fluorescence intensity, with an increased ratio indicating elevated lipid ROS levels.

Endoplasmic Reticulum Staining

The endoplasmic reticulum (ER) in primary cardiomyocytes was labeled using ER-Tracker™ Green (40763ES20, Yeasen Biotechnology, Shanghai, China). The stock solution (1 mM in DMSO) was diluted in pre-warmed, serum-free medium under light-protected conditions to a final working concentration of 100 nM. Following the indicated treatments, cardiomyocytes were gently washed three times with pre-warmed phosphate-buffered saline (PBS). Cells were then incubated with the ER-Tracker™ Green working solution at 37°C in a humidified atmosphere containing 5% CO_2 for 20–30 min in the dark. After staining, the dye solution was removed, and cells were washed three times with pre-warmed PBS to remove excess probe. Stained cells were immediately imaged using a laser scanning confocal microscope with excitation at 488 nm, and fluorescence emission was collected in the 500–540 nm spectral range.

Thioflavin T Staining

Primary cardiomyocytes were fixed in 4% paraformaldehyde and permeabilized with 0.1% Triton X-100 in phosphate-buffered saline (PBS). After washing three times with PBS, cells were incubated with Thioflavin T (MedChemExpress, HY-D0218, Monmouth Junction, NJ, USA) for 20 min at 37°C to label misfolded protein aggregates. Following staining, cells were washed three times with PBS and counterstained with DAPI (C1006, Beyotime, Shanghai, China) for 5 min to visualize nuclei. Cells were then washed three times with pre-warmed PBS, mounted using an antifade mounting medium, and immediately imaged using a laser scanning confocal microscope with excitation at 488 nm and appropriate emission filters.

Protein Extraction and Western Blot Analysis (WB)

Total protein from cardiomyocytes and cardiac tissues was extracted using RIPA lysis buffer (P0013B, Beyotime, Shanghai, China) supplemented with phenylmethylsulfonyl fluoride (PMSF; ST506, Beyotime, Shanghai, China). Protein concentrations were determined using a standard assay, and equal amounts of protein were resolved by SDS–PAGE and transferred onto polyvinylidene fluoride (PVDF) membranes.

Membranes were blocked in Tris-buffered saline containing 5% non-fat milk and incubated overnight at 4°C with primary antibodies, with β-actin used as an internal loading control. After washing with Tris-buffered saline containing 0.1% Tween-20 (TBST), membranes were incubated with horseradish peroxidase–conjugated secondary antibodies (anti-rabbit IgG, 7074; anti-mouse IgG, 7076; both 1:2000; Cell Signaling Technology, Boston, MA, USA) for 1 h at room temperature. Protein bands were visualized using an enhanced chemiluminescence detection system and quantified using appropriate image analysis software.

Antibodies Used for Immunoblot Analysis

RPS5 Polyclonal antibody (16964-1-AP), ACOX1 Polyclonal antibody (10957-1-AP), GPD1 Polyclonal antibody (13451-1-AP), Glycerokinase Polyclonal antibody (13360-1-AP), DLAT Polyclonal antibody (13426-1-AP), FBP2 Polyclonal antibody (25192-1-AP), Hexokinase 1 Polyclonal antibody (19662-1-AP), PFKM Polyclonal antibody (55028-1-AP), G6PD Polyclonal antibody (25413-1-AP), FAH Polyclonal antibody (14928-1-AP), IDO1 Polyclonal antibody (13268-1-AP), HADH Polyclonal antibody (19828-1-AP), ATP5A1 Polyclonal antibody (14676-1-AP), UQCRC2 Polyclonal antibody (14742-1-AP), NDUFB8 Polyclonal antibody (14794-1-AP), SDHB

Polyclonal antibody (10620-1-AP), GRP78/BIP Polyclonal antibody (11587-1-AP), ATF4 Polyclonal antibody (10835-1-AP), CHOP Polyclonal antibody (15204-1-AP), HSP60 Polyclonal antibody (15282-1-AP), LONP1 Polyclonal antibody (15440-1-AP), CLPP Polyclonal antibody (15698-1-AP), TOMM40 Polyclonal antibody (18409-1-AP), Mouse Monoclonal anti FLAG (66008 4 Ig), Beta Actin Polyclonal antibody (20536-1-AP) were purchased from Proteintech. MPRPS5 Polyclonal antibody (GTX103930) was purchased from GeneTex. RPS5 Polyclonal antibody (sc 100832), BAP31 Polyclonal antibody (sc 393810) were purchased from Santa Cruz Biotechnology. The vast majority of primary antibodies included in the study were diluted at 1:1000 in 5% bovine serum albumin (BSA), except anti-β-actin (1:10,000 dilution), and anti-Flag-Tag (1:20,000 dilution).

Measurement of Protein Synthesis Rate

Global protein synthesis in cardiomyocytes was assessed using a puromycin incorporation assay. Primary cardiomyocytes were cultured in normal-glucose (NG; 5.5 mM) or high-glucose (HG; 33 mM) medium for 48 h. Following treatment, cells were incubated with fresh corresponding medium containing puromycin (10 μg/mL; MedChemExpress, HY-K1057, Monmouth Junction, NJ, USA) for 30 min at 37°C in a humidified atmosphere with 5% CO_2. After incubation, cells were washed twice with ice-cold phosphate-buffered saline (PBS), rapidly collected, and lysed in RIPA lysis buffer supplemented with protease inhibitors on ice for 30 min. Lysates were clarified by centrifugation at 12,000 × g for 15 min at 4°C, and protein concentrations were determined and normalized across samples. Puromycin incorporation into nascent polypeptides was detected by Western blotting using an anti-puromycin monoclonal antibody (A23031, ABclonal, Wuhan, China), with β-actin serving as a loading control. Relative puromycin signal intensities were quantified to assess global protein synthesis rates under different glucose conditions.

RNA Extraction and Agarose Gel Electrophoresis

Total RNA from cardiomyocytes was extracted using the TransZol Up Plus RNA Kit (ER501-01-V2, TransGen Biotech, Beijing, China) according to the manufacturer's instructions. RNA concentration and purity were assessed spectrophotometrically prior to downstream analyses.

For RNA integrity assessment, a 1% agarose gel was prepared by dissolving 0.5 g agarose (BS081, Biosharp, China) in 50 mL of 1× TAE buffer (143281, Biosharp, China). The solution was heated until fully dissolved, cooled to approximately 60 °C, and supplemented with GelRed nucleic acid stain (5 μL; 41003, Biotium, USA). The gel was poured into a casting tray with a comb and allowed to solidify at room temperature for 30 min.

For each sample, 1 μg of total RNA was mixed with an equal volume of 2× RNA loading buffer (R0215, Beyotime, Shanghai, China) and loaded into the wells. A single-stranded RNA ladder (N0362S, New England Biolabs, USA) was run in parallel for size reference. Electrophoresis was performed in 1× TAE buffer at a constant voltage of 5 V/cm for approximately 30 min. Gels were imaged using a gel documentation system under blue-light excitation. RNA integrity was evaluated based on the sharpness and intensity of the 28S and 18S ribosomal RNA bands, with an expected 28S:18S intensity ratio of approximately 2:1 in intact RNA and minimal evidence of degradation or smearing.

Immunofluorescence

Primary cardiomyocytes cultured on glass coverslips were fixed with 4% paraformaldehyde for 15 min at room temperature, washed three times with phosphate-buffered saline (PBS), and permeabilized with 0.1% Triton X-100 in PBS for 10 min.

Cells were then washed and blocked with 5% bovine serum albumin (BSA) in PBS for 1 h at room temperature to reduce nonspecific binding. Cells were incubated overnight at 4°C with the indicated combinations of primary antibodies diluted in blocking buffer. After three washes with PBS, cells were incubated for 1 h at room temperature in the dark with species-specific secondary antibodies conjugated to distinct fluorophores (Alexa Fluor 488, 555, 594, 647; Invitrogen), allowing simultaneous four-color detection. Following secondary antibody incubation, nuclei were counterstained with DAPI for 5 min. Coverslips were washed thoroughly with PBS and mounted using antifade mounting medium. Fluorescence images were acquired using a laser scanning confocal microscope (Leica STELLARIS 8) equipped with appropriate excitation lasers and emission filters.

All images were collected using identical acquisition settings within each experiment. Colocalization analysis was performed using ImageJ software with the Coloc2 plugin, and Pearson's correlation coefficients were calculated where indicated. At least three independent biological replicates were analyzed for each condition.

Mitochondrial Stress Test (Seahorse XF Assay)

Mitochondrial respiratory function was assessed using a Seahorse XF extracellular flux analyzer. Primary cardiomyocytes were seeded at a density of approximately 20,000 cells per well in Seahorse XF cell culture microplates and cultured for 48 h to allow formation of a uniform monolayer. Prior to the assay, culture medium was replaced with pre-warmed, unbuffered Seahorse XF RPMI medium supplemented with 10 mM glucose, 2 mM glutamine, and 1 mM sodium pyruvate. Plates were incubated in a non-CO_2 incubator at 37°C for 1 h to allow equilibration of temperature and pH. The Seahorse sensor cartridge was hydrated overnight and calibrated using a Seahorse XFe24 Analyzer (Agilent Technologies, Beijing, China).

Following calibration, compounds were sequentially injected through the instrument's automated ports as follows: oligomycin (1.5 μM), carbonyl cyanide *p*-trifluoromethoxyphenylhydrazone (FCCP; 2 μM), and a mixture of rotenone and antimycin A (0.5 μM). Oxygen consumption rate (OCR) was recorded in real time throughout the assay. After completion of the experiment, viable cell numbers in each well were quantified and used to normalize OCR values. All reagents for the mitochondrial stress test were obtained from Agilent Technologies.

Biochemistry Measurements

Blood samples were collected from mice in each experimental group by cardiac puncture. Plasma was isolated by centrifugation and used to measure levels of total cholesterol (TC), triglycerides (TG), high-density lipoprotein cholesterol (HDL-c), and low-density lipoprotein cholesterol (LDL-c).Plasma lipid concentrations were determined using commercially available assay kits from Nanjing Jiancheng Bioengineering Institute (Nanjing, China): TG assay kit (A11011), TC assay kit (A11111), HDL-c assay kit (A11211), and LDL-c assay kit (A11311), according to the manufacturers' instructions.

Molecular Docking

Protein–protein docking was performed using mouse MRPS5 (UniProt ID: Q99N87) and RPS5 (UniProt ID: P97461). Predicted protein structures were obtained from the AlphaFold Protein Structure Database (https://alphafold.ebi.ac.uk/). Molecular docking was conducted using the HDOCK server (http://hdock.phys.hust.edu.cn/).

Binding free energy calculations for the resulting protein–protein complexes were carried out using the MM/GBSA method implemented in the HawkDock server (http://cadd.zju.edu.cn/hawkdock/). Amino acid residues at the interaction interface were ranked based on their contributions to binding free energy. The docking score was

used to select the optimal docking model from the generated conformations, and the corresponding binding free energy was calculated. The top-ranked interaction interfaces and key residues were visualized using PyMOL software (version 2.4).

Co-Immunoprecipitation (Co-IP)

Expression vectors encoding mouse RPS5 or MRPS5 with C-terminal 3×FLAG tags (pCDH-CMV-RPS5-3×FLAG-CopGFP-Puro and pCDH-CMV-MRPS5-3×FLAG-CopGFP-Puro) were constructed by Wz Biosciences Inc. (Shandong, China). All plasmids were verified by DNA sequencing to confirm correct coding sequences and reading frames.

Primary cardiomyocytes were transfected with the indicated plasmids using Lipofectamine 2000 (Invitrogen) and harvested 48 h after transfection. Cells were lysed on ice for 30 min using a mild lysis buffer (P0013, Beyotime, Shanghai, China), followed by centrifugation at 12,000 × g for 15 min at 4°C. The supernatants were collected as total protein extracts.

Equal amounts of protein were incubated with Protein A/G magnetic beads (MedChemExpress, HY-K0202, Monmouth Junction, NJ, USA) overnight at 4°C with gentle rotation. Beads were washed five times with lysis buffer to remove nonspecifically bound proteins. Bound proteins were eluted by boiling in 1× SDS–PAGE loading buffer at 95°C for 10 min. Eluted proteins were resolved by SDS–PAGE and analyzed by Western blotting.

Statistical Analysis

Data are presented as mean ± SEM. Unless otherwise indicated, statistical analyses were performed using GraphPad Prism 10 (GraphPad Software Inc., San Diego, CA, USA). Prior to hypothesis testing, data distributions were assessed for normality using the Shapiro–Wilk test.

For normally distributed data, comparisons between two groups were performed using an unpaired two-tailed Student's *t*-test. Comparisons among multiple groups were analyzed using one-way analysis of variance (ANOVA) followed by Tukey's multiple-comparison post hoc test, while experiments involving two independent variables were analyzed using two-way ANOVA with Tukey's post hoc correction. For data that did not meet normality assumptions, appropriate nonparametric tests were applied as specified in the figure legends.

Details of the statistical tests used, exact *p* values, and sample sizes are provided in the corresponding figure legends. Statistical significance was defined as $p < 0.0$, $p < 0.01$, and $p < 0.001$; ns indicates no statistically significant difference. The value of *n* represents the number of individual animals for in vivo experiments or the number of independent biological replicates for in vitro experiments. Unless otherwise stated, all in vitro experiments were performed with at least three independent biological replicates.

SUPPLEMENTAL INFORMATION

Supplemental information is provided.

Figures

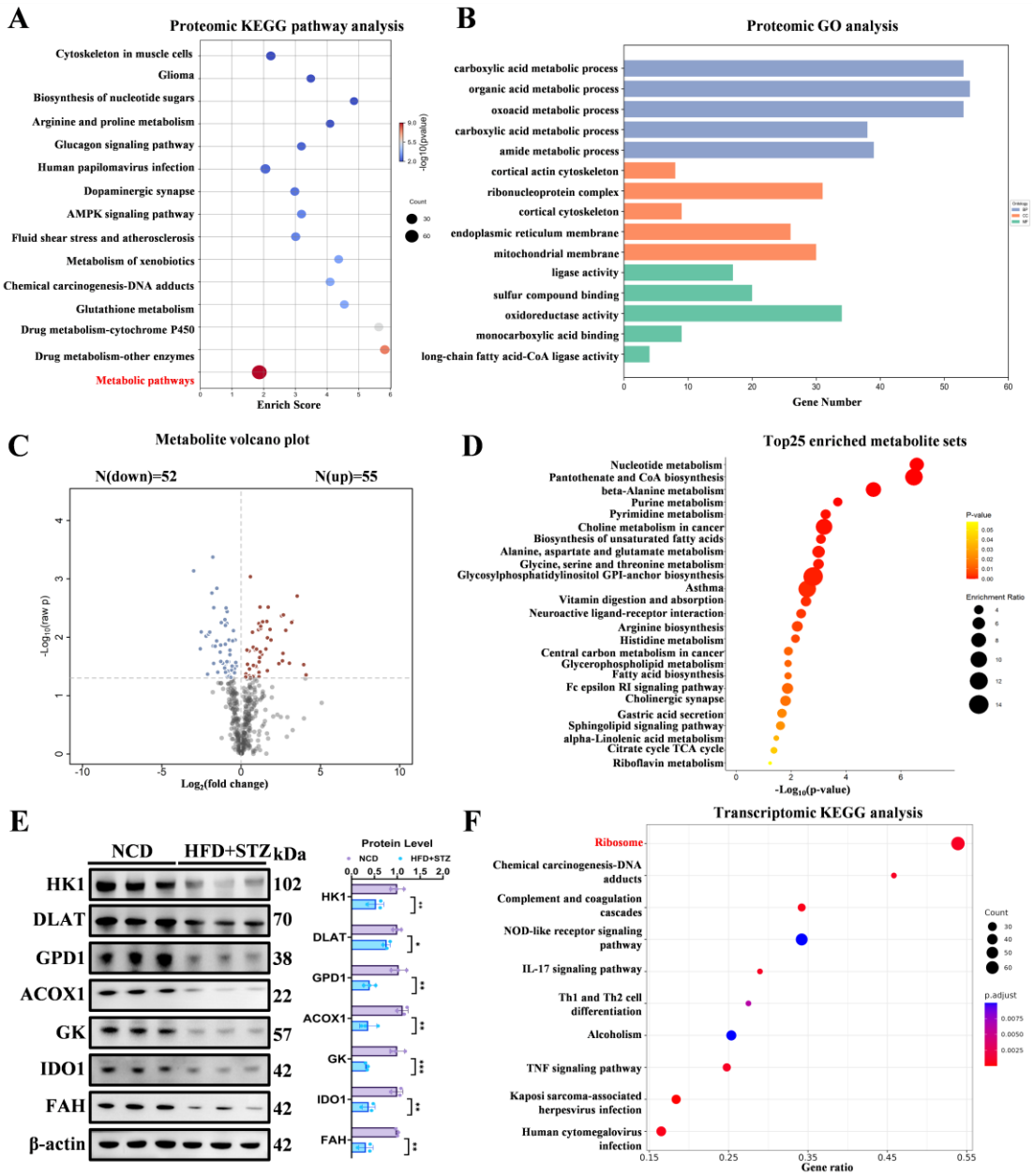

Figure 1. Multi-omics profiling identifies coordinated metabolic and ribosomal remodeling in the diabetic heart. Metabolic dysfunction in DCM is accompanied by a coordinated collapse of ribosomal systems, revealing a previously unrecognized translational defect. **(A)** Bubble plot of KEGG pathway enrichment analysis based on integrated proteomic data from control and DCM hearts (n = 3 per group). The x-axis indicates the enrichment score, bubble size represents the number of molecules mapped to each pathway, and bubble color denotes statistical significance ($-\log_{10}$ p value). Metabolic pathways are prominently enriched, highlighting broad metabolic reprogramming in the diabetic heart. **(B)** Gene Ontology (GO) enrichment analysis of differentially expressed proteins in DCM hearts compared to controls (n = 3 per group). Bar plots show significantly enriched biological processes (BP), cellular components (CC), and molecular functions (MF). Metabolic processes dominate the BP category, whereas enrichment of ribonucleoprotein complex, endoplasmic reticulum membrane, and mitochondrial membrane components indicates coordinated alterations in protein

synthesis and organelle homeostasis. **(C)** Volcano plot of cardiac metabolomic data (DCM over control), with x-axis representing the $\log_2$-transformed fold change, and the y-axis representing the -$\log_{10}$–transformed *p*-value (adjusted using the Benjamini-Hochberg method for multiple comparisons). Each data point corresponds to an individual metabolite. Red dots indicate metabolites that are significantly upregulated (fold change > 1 and adjusted *p*-value < 0.05), whereas blue dots indicate metabolites that are significantly downregulated (fold change < 1 and adjusted *p*-value < 0.05). A total of 55 upregulated and 52 downregulated metabolites were identified. **(D)** Metabolite set enrichment analysis of cardiac metabolomics data ($n = 3$ per group). The dot plot displays the top 25 enriched metabolite sets ranked by $-\log_{10}$ (*p* value). Dot size represents the enrichment ratio, and dot color indicates statistical significance. Multiple central metabolic pathways, including nucleotide, amino acid, purine, and riboflavin metabolism, are significantly altered in DCM hearts. **(E)** Representative immunoblots showing altered expression of key metabolic enzymes, ribosomal proteins, and stress-response markers in control and DCM hearts ($n = 3$ independent biological replicates). B-actin served as a loading control. Right panel: quantification of selected metabolic and stress-related protein expression levels from immunoblot analyses. Data are presented as mean ± SEM. **(F)** KEGG pathway enrichment analysis of transcriptomic data from DCM hearts ($n = 3$ per group). While metabolic pathways are less prominently enriched at the transcript level, pathways related to ribosome function, inflammatory signaling (including TNF and IL-17 signaling), immune responses, and stress-associated pathways are significantly represented. Dot size reflects gene count, and dot color indicates adjusted *p*-value, highlighting the discordance between transcriptional and proteomic/metabolomic regulation. Statistical significance was determined using the tests described in the Methods section. $*p < 0.05$, $**p < 0.01$, and $***p < 0.001$. ns, not significant. Abbreviations: DCM, diabetic cardiomyopathy; DBDB, a genetically engineered mouse strain used as a standard model for T2DM; NCD, normal control diet; HFD, high-fat diet; STZ, streptozotocin; HFD+STZ, male C57BL/6 mice fed an HFD followed by intraperitoneal STZ injection to establish an experimental model of T2DM.

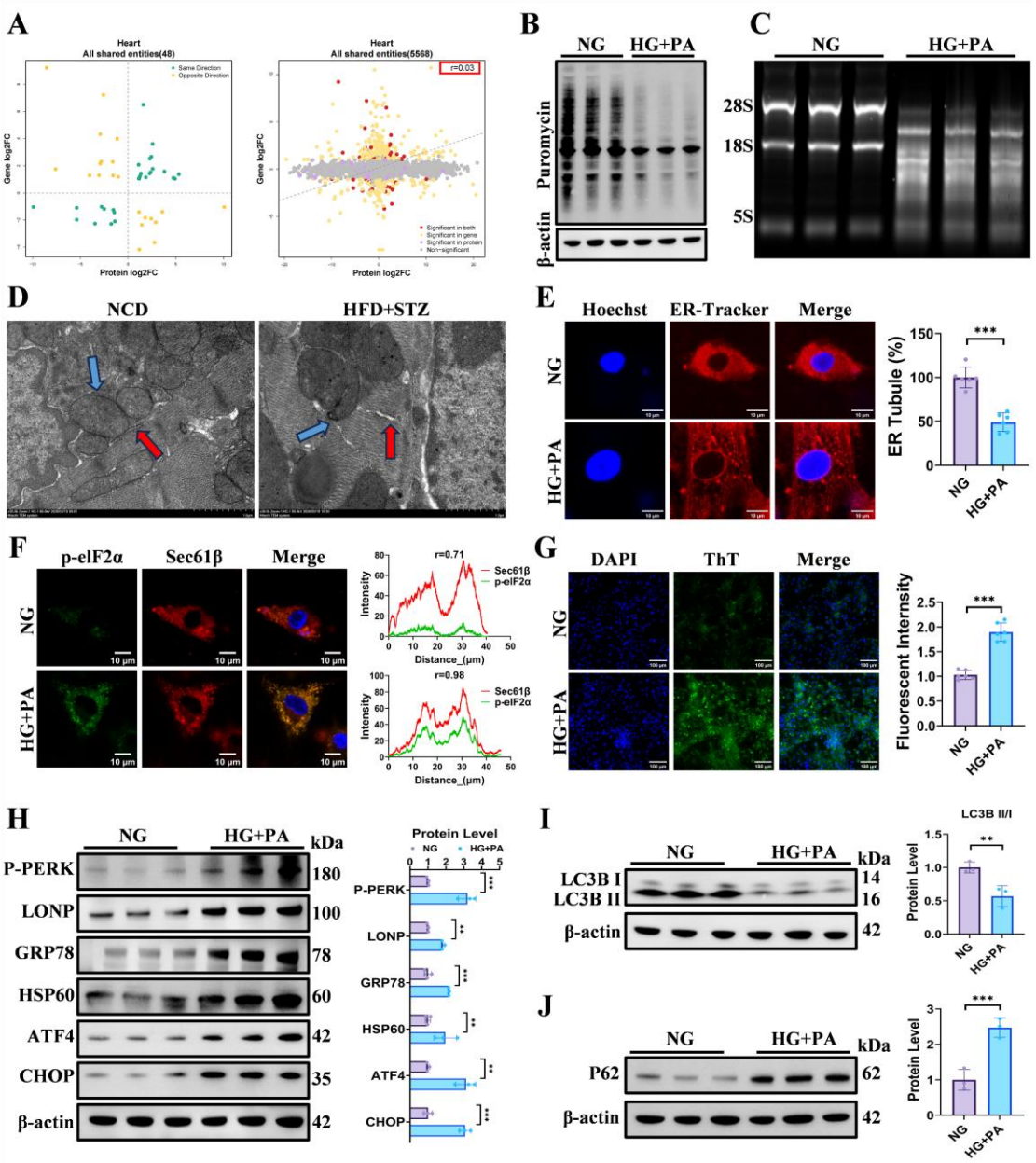

Figure 2. Global translational suppression drives proteostasis collapse and underlie discordance between transcriptomic and proteomic regulation in diabetic hearts. Diabetic stress induces global translational suppression that drives ER disruption and proteostasis collapse, explaining the disconnect between transcriptomic and proteomic regulation. **(A)** Scatter plots comparing fold changes at the transcriptomic (y-axis, gene log_2FC) and proteomic (x-axis, protein log_2FC) levels in heart tissue from diabetic cardiomyopathy mice versus controls (n = 3 per group). Left panel: entities significantly altered at both gene and protein levels (n = 48), color-coded by concordant (same direction) or discordant (opposite direction) regulation. Right panel: all shared entities (n = 5,568), highlighting a weak overall correlation between mRNA and protein abundance (Pearson's r = 0.03), indicating extensive post-transcriptional dysregulation in the diabetic heart. **(B)** Representative immunoblot of puromycin incorporation assay (SUnSET) showing global protein synthesis rates in cardiomyocytes under control and diabetic conditions (n = 3 independent biological replicates). Reduced puromycin incorporation indicates suppressed translational activity. β-actin serves as a loading control. **(C)** Agarose gel electrophoresis of total

RNA extracted from cardiomyocytes under control and diabetic conditions (n = 3 independent biological replicates). Diabetic samples exhibit reduced total RNA content, with the 28S and 18S rRNA bands appearing faint and poorly defined, consistent with impaired ribosome biogenesis and global translational deficiency. **(D)** Transmission electron microscopy (TEM) images of cardiomyocytes from normal and diabetic mice. Blue arrows indicate mitochondria, and red arrows indicate rough endoplasmic reticulum (RER). Left panel: in normal mouse cardiomyocytes, the RER exhibits intact structural integrity with ribosomes attached to the membranes and maintains close contact with mitochondria. Right panel: in diabetic mouse cardiomyocytes, the RER loses its structural integrity, characterized by swelling and dilation of the RER cisternae, partial detachment of ribosomes from the membranes, and reduced contact with mitochondria, as evidenced by increased inter-organellar distance. Scale bar, 1 μm (n = 3 mice per group). **(E)** Representative immunofluorescence images showing endoplasmic reticulum (ER) morphology in cardiomyocytes stained with ER-Tracker (red) and nuclei counterstained with Hoechst (blue) (n = 6 independent biological replicates). Diabetic conditions induce fragmentation and loss of the continuous ER network compared with controls. Scale bars, 10 μm. Right panel: quantification of the percentage of ER tubules. **(F)** Representative immunofluorescence images showing co-localization of phosphorylated eIF2α (p-eIF2α, green) and the rough endoplasmic reticulum translocon component Sec61β (red) in cardiomyocytes under control and diabetic conditions (n = 6 independent biological replicates). Scale bars, 10 μm. Right panel: quantitative colocalization analysis using ImageJ, demonstrating a significantly higher Pearson's correlation coefficient for p-eIF2α and Sec61β under diabetic conditions compared with controls (0.98 vs. 0.71), indicative of elevated ER-associated translational stress. **(G)** Representative immunofluorescence images of cardiomyocytes stained with Thioflavin T (ThT; green) and nuclei counterstained with DAPI (blue) to detect protein aggregates (n = 6 independent biological replicates). Scale bars, 100 μm. Right panel: quantitative analysis of Thioflavin T fluorescence, revealing a marked elevation in protein aggregates under diabetic conditions compared with controls. **(H)** Representative western blot analyses of ER stress markers, translational stress markers, and mitochondrial proteostasis regulators in cardiomyocytes under control and diabetic conditions (n = 3 independent biological replicates), demonstrating activation of the unfolded protein response and proteotoxic stress. Right panel: quantification of ER stress and proteostasis-related protein expression. **(I)** Representative western blot analyses of LC3B-II/I ratio in cardiomyocytes under control and diabetic conditions (n = 3 independent biological replicates). Right panel: quantification of LC3B-II/I ratio. **(J)** Representative western blot analyses of P62 in cardiomyocytes under control and diabetic conditions (n = 3 independent biological replicates). Right panel: quantification of P62 protein expression. Statistical significance was determined using the tests described in the Methods. All data are presented as mean ± SEM. *$p < 0.05$, **$p < 0.01$, and ***$p < 0.001$. Abbreviations: NG, normoglycemic culture conditions; HG, hyperglycemic culture conditions; PA, palmitic acid; HG+PA, hyperglycemic culture conditions supplemented with PA to mimic T2DM at the cellular level; ThT, Thioflavin T.

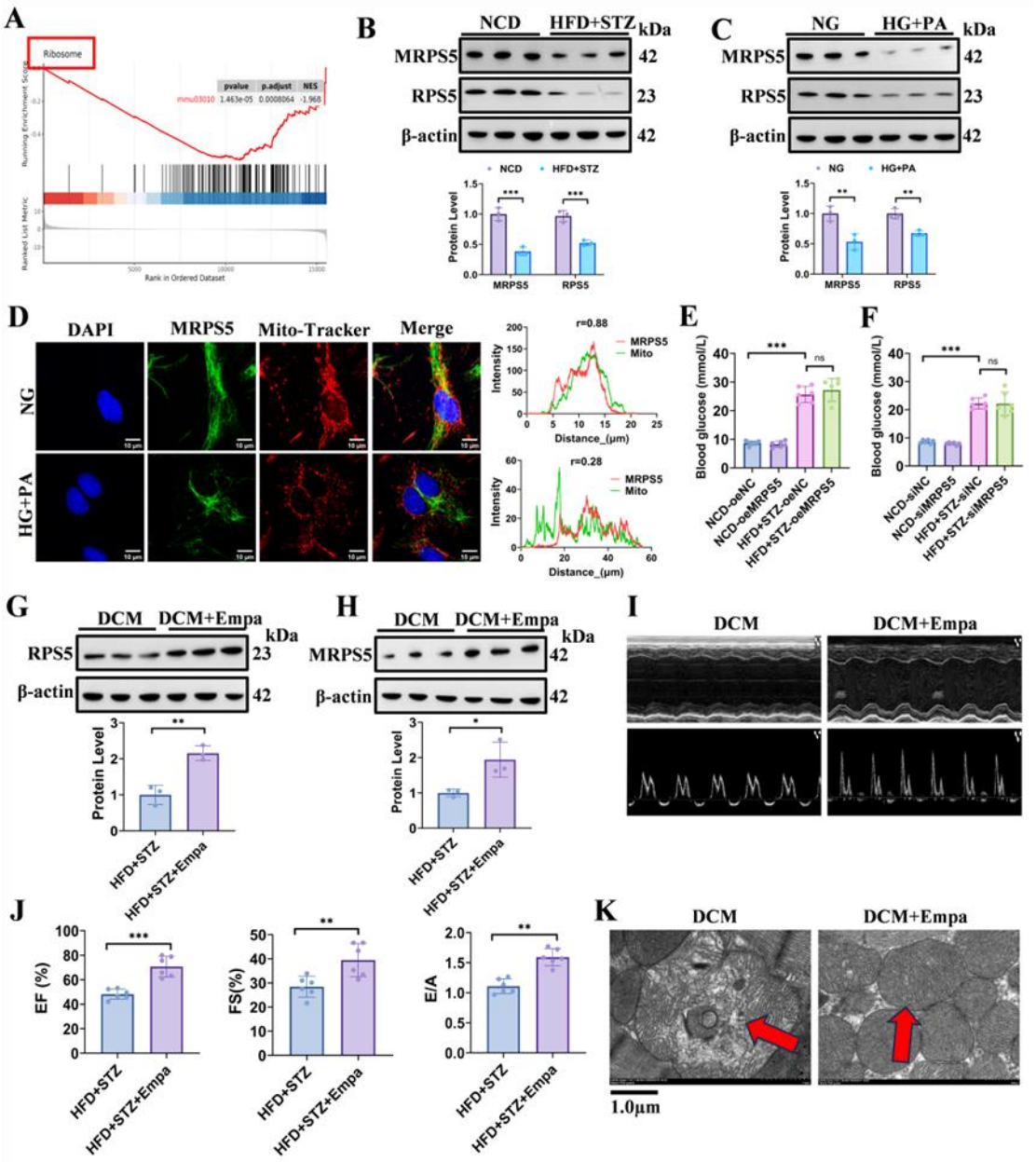

Figure 3. Diabetic stress suppresses cytosolic and mitochondrial ribosomal programs and impairs MRPS5 mitochondrial localization. Diabetic stress induces coordinated suppression of cytosolic and mitochondrial ribosomal programs and impairs MRPS5 mitochondrial localization, defining a primary defect in translational capacity. **(A)** Gene Set Enrichment Analysis (GSEA) demonstrating significant negative enrichment of the ribosome pathway in DCM hearts (n = 3). The running enrichment score plot indicates global suppression of ribosomal components and translational machinery in the diabetic myocardium (normalized enrichment score and adjusted p value are shown). **(B)** Representative Western blot analysis of mitochondrial ribosomal protein MRPS5 and cytoplasmic ribosomal protein RPS5 in control and DCM hearts (n = 3). Reduced expression of both ribosomal proteins confirms proteomic findings. β-actin serves as a loading control. Right panel: quantification of ribosomal protein expression levels. **(C)** Representative Western blot analysis of selected ribosomal proteins and translational regulators in cardiomyocytes under control and diabetic conditions in primary cultured mouse cardiomyocytes high-glucose medium (HG; 33 mM glucose) supplemented with palmitic acid (PA; 0.2 mM)

(n = 3). Right panel: quantification of ribosomal protein expression levels. Reduced expression of ribosomal components under diabetic conditions confirms translational suppression. β-actin serves as a loading control. **(D)** Representative immunofluorescence images showing the subcellular localization of MRPS5 (green) and mitochondria (Mito-Tracker, red) in cardiomyocytes cultured under control and diabetic conditions. Nuclei were counterstained with DAPI (blue) (n = 6). Scale bars, 10 μm. Merged images reveal reduced mitochondrial localization of MRPS5 under diabetic conditions. The right panel shows the fluorescence intensity profiles of MRPS5 and Mito-Tracker, with Pearson's correlation coefficients quantifying the degree of co-localization (NG: r = 0.95; HG+PA: r = 0.88). **(E)** The data showed a significant increase in blood glucose levels in diabetic cardiomyopathy mice compared with normal controls, whereas no significant alteration in blood glucose was observed in DCM mice following MRPS5 overexpression (n = 6). **(F)** The data showed a significant increase in blood glucose levels in diabetic cardiomyopathy mice compared with normal controls, whereas no significant alteration in blood glucose was observed in DCM mice following MRPS5 knockdown (n = 6). **(G)** Representative Western blot analyses of RPS5 under DCM, and DCM+Empagliflozin mice (n = 3). Bottom panel: Quantification of RPS5 protein expression. **(H)** Representative Western blot analyses of MRPS5 under DCM, and DCM+Empagliflozin mice (n = 3). Bottom panel: Quantification of MRPS5 protein expression. **(I)** Representative transthoracic echocardiographic M-mode (upper panels) and transmitral Doppler flow (lower panels) images from diabetic cardiomyopathy (DCM; HFD+STZ) mice with or without empagliflozin treatment (Empa). Empagliflozin markedly improved left ventricular systolic wall motion and chamber dynamics, and partially restored diastolic filling patterns compared with untreated DCM mice. **(J)** Quantitative echocardiographic analysis showing that empagliflozin significantly increased ejection fraction (EF%), fractional shortening (FS%), and the E/A ratio relative to untreated DCM mice, indicating improved systolic and diastolic cardiac performance. **(K)** Representative transmission electron microscopy images of myocardial tissue from DCM mice with or without empagliflozin treatment. Untreated DCM hearts exhibited swollen and structurally disorganized mitochondria with disrupted cristae architecture (arrow), whereas empagliflozin preserved mitochondrial morphology and ultrastructural integrity, with more compact mitochondria and better-organized cristae (arrow). Statistical significance was determined using the tests described in the Methods. All data are presented as mean ± SEM. *p < 0.05, **p < 0.01, and ***p < 0.001. Abbreviations: NG, normoglycemic culture conditions; HG, hyperglycemic culture conditions; PA, palmitic acid; HG+PA, hyperglycemic culture conditions supplemented with PA to mimic T2DM at the cellular level; STZ, streptozotocin; HFD+STZ, male C57BL/6 mice fed with a high-fat diet followed by intraperitoneal injection of STZ to establish an experimental model of T2DM; Mito, mitochondria; siNC, negative control siRNA; siRPS5, RPS5-targeting siRNA; siMRPS5, MRPS5-targeting siRNA; oeNC, empty vector control; oeRPS5, RPS5 overexpression; oeMRPS5, MRPS5 overexpression; EF, ejection fraction; FS, fractional shortening; E/A ratio, E wave (Early diastolic filling)/A wave (Atrial contraction filling); Empa, Empagliflozin.

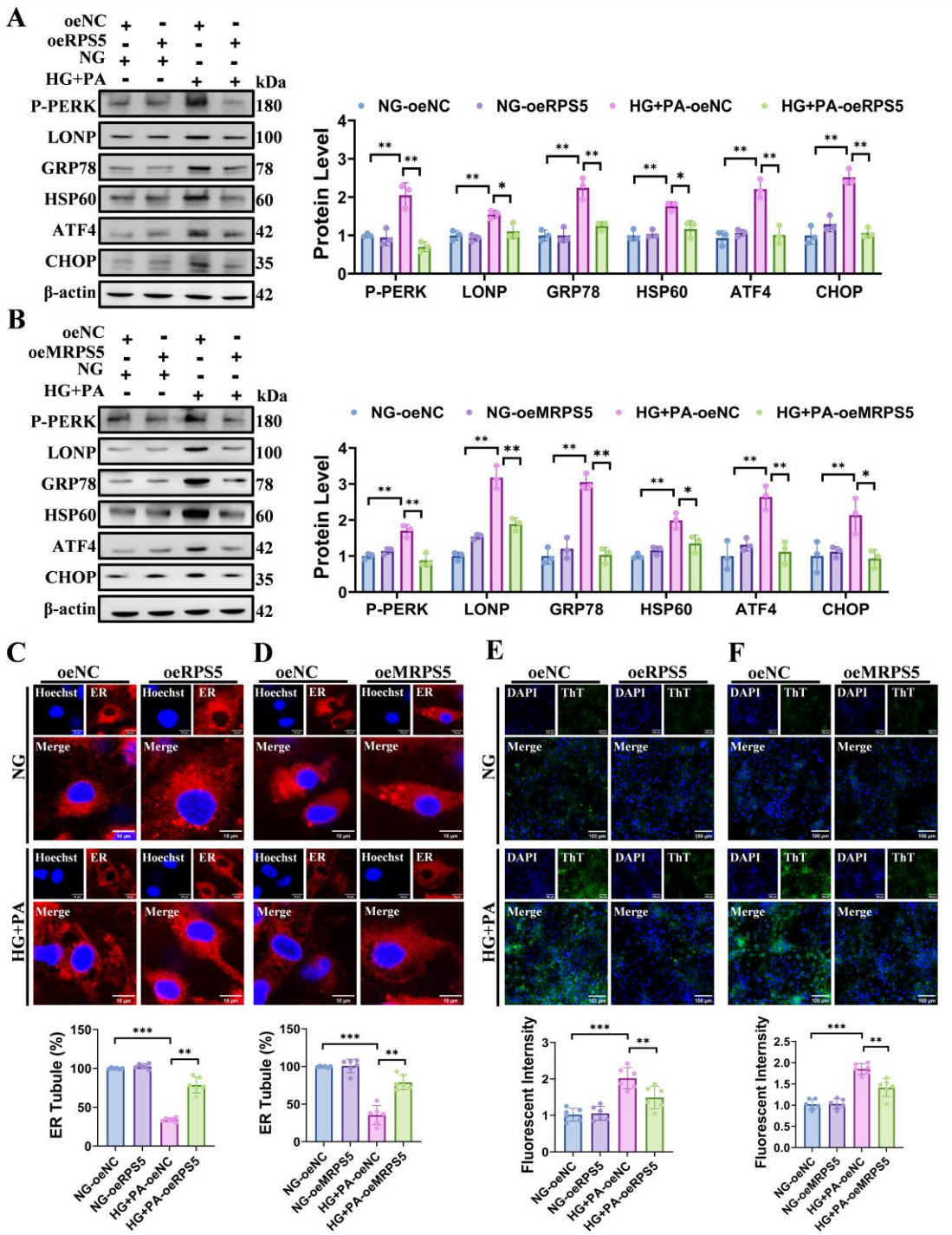

Figure 4. Restoration of RPS5 and MRPS5 rescues proteostasis, ER integrity, and metabolic remodeling. Restoration of RPS5 or MRPS5 alleviates proteostasis stress and restores ER structural integrity in cardiomyocytes exposed to diabetic conditions. **(A, B)** Representative immunoblot analyses of proteostasis stress markers in cardiomyocytes under normoglycemic (NG) or diabetic (HG+PA) conditions with overexpression of RPS5 (A) or MRPS5 (B) in cardiomyocytes transfected with empty vector control (oeNC) or RPS5/MRPS5 overexpression plasmid (oeRPS5/oeMRPS5). Proteins analyzed include ER stress markers (P-PERK, GRP78, ATF4, CHOP) and mitochondrial proteostasis regulators (LONP, HSP60). β-actin serves as a loading control. Right panels: quantification of protein expression levels normalized to β-actin (n = 3 independent biological replicates). **(C, D)** Representative immunofluorescence

images of endoplasmic reticulum (ER) morphology in cardiomyocytes stained with ER-Tracker (red) and nuclei counterstained with Hoechst (blue) under NG or HG+PA conditions with overexpression of RPS5 (C) or MRPS5 (D) (n = 6). Diabetic conditions induce ER fragmentation and disruption of the tubular network, which is partially restored upon RPS5 or MRPS5 overexpression. Bottom panels: quantitative analysis of ER tubule integrity. Scale bars, 10 μm. **(E, F)** Representative immunofluorescence images of protein aggregation assessed by Thioflavin T (ThT; green) staining in cardiomyocytes under NG or HG+PA conditions with overexpression of RPS5 (E) or MRPS5 (F). Nuclei are counterstained with DAPI (blue) (n = 6). Diabetic stress markedly increases protein aggregation, which is attenuated by RPS5 or MRPS5 overexpression. Bottom panels: quantification of ThT fluorescence intensity. Scale bars, 100 μm. Statistical significance was determined using the tests described in the Methods. All data are presented as mean ± SEM. $*p < 0.05$, $**p < 0.01$, $***p < 0.001$. Abbreviations: NG, normoglycemic culture conditions; HG, hyperglycemic culture conditions; PA, palmitic acid; HG+PA, hyperglycemic culture conditions supplemented with PA to mimic T2DM at the cellular level; oe, overexpression; NC, negative control with blank plasmid.

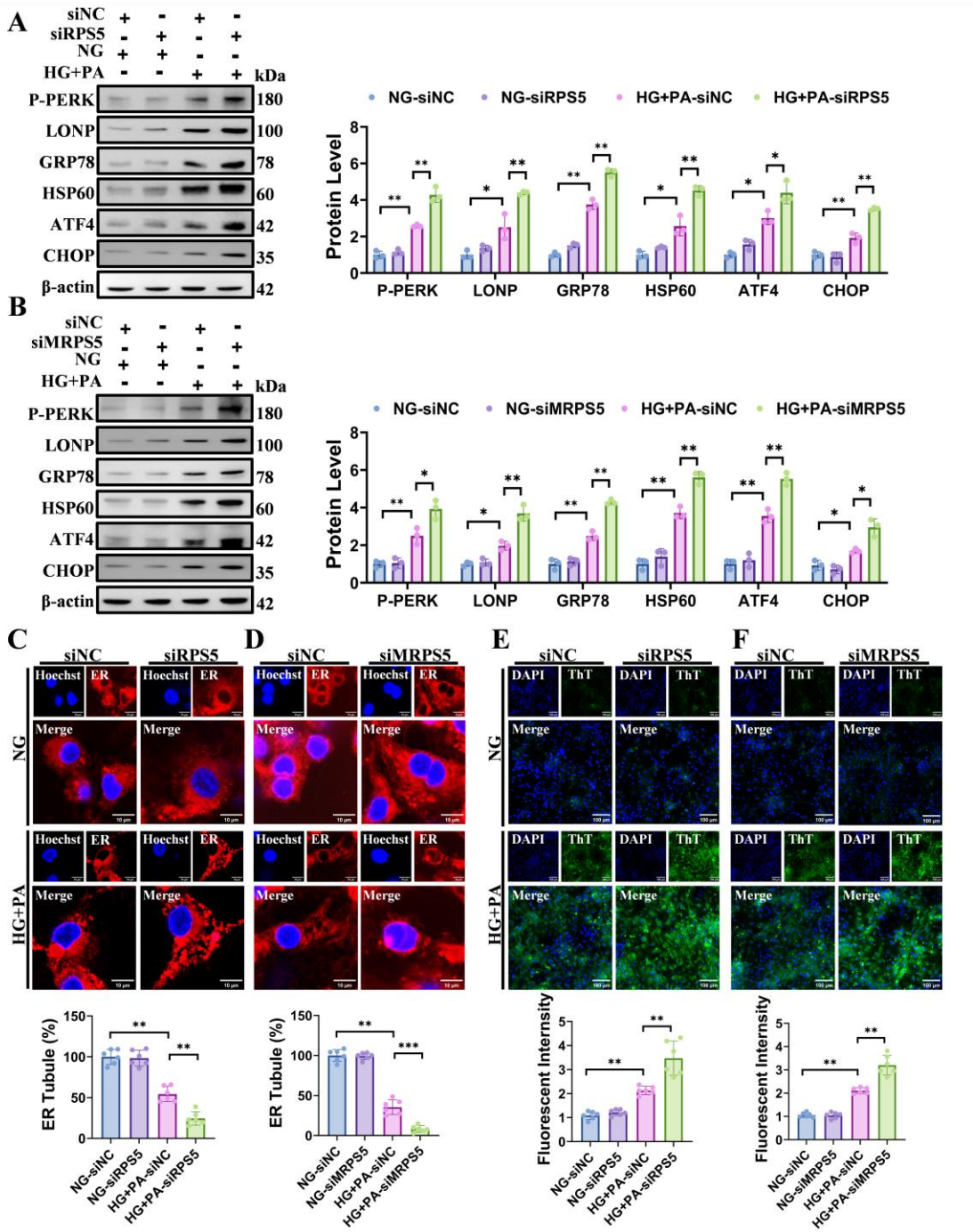

Figure 5. RPS5 and MRPS5 maintain proteostasis and ER integrity in diabetic cardiomyocytes. RPS5–MRPS5 deficiency exacerbates ER stress, protein aggregation, and proteostasis failure under diabetic conditions. **(A)** Representative immunoblot analysis of proteostasis stress markers, including ER stress and mitochondrial proteostasis regulators, in cardiomyocytes under diabetic conditions following knockdown of RPS5 expression compared with negative control (n = 3). Right panel: quantification of protein expression levels. **(B)** Representative immunoblot analysis of proteostasis stress markers, including ER stress and mitochondrial proteostasis regulators, in cardiomyocytes under diabetic conditions following knockdown of MRPS5 expression compared with negative control (n = 3). Right panel: quantification of protein expression levels. **(C)** Representative immunofluorescence images showing endoplasmic reticulum (ER) morphology in cardiomyocytes stained with ER-Tracker (red) and nuclei counterstained with Hoechst (blue) under control or diabetic conditions

with or without RPS5 knockdown ($n = 6$). Scale bars, 10 μm. Bottom panel: quantitative analysis of ER tubule morphology. **(D)** Representative immunofluorescence images of cardiomyocytes stained with Thioflavin T (green) and nuclei counterstained with DAPI (blue) to detect protein aggregates under control or diabetic conditions with or without RPS5 knockdown ($n = 6$). Scale bars, 100 μm. Bottom panel: quantitative analysis of Thioflavin T fluorescence, revealing that RPS5 knockdown significantly exacerbates the accumulation of protein aggregates induced by diabetic conditions. **(E)** Representative immunofluorescence images showing endoplasmic reticulum (ER) morphology in cardiomyocytes stained with ER-Tracker (red) and nuclei counterstained with Hoechst (blue) under control or diabetic conditions with or without MRPS5 knockdown ($n = 6$). Scale bars, 10 μm. Bottom panel: quantitative analysis of ER tubule morphology, revealing that MRPS5 knockdown further aggravates high-glucose/high-palmitic acid-induced fragmentation and disruption of the continuous ER network. **(F)** Representative immunofluorescence images of cardiomyocytes stained with Thioflavin T (green) and nuclei counterstained with DAPI (blue) to detect protein aggregates under control or diabetic conditions with or without MRPS5 knockdown ($n = 6$). Scale bars, 100 μm. Bottom panel: quantitative analysis of Thioflavin T fluorescence, revealing that MRPS5 knockdown significantly exacerbates the accumulation of protein aggregates induced by diabetic conditions. Statistical significance was determined using the tests described in the Methods. All data are presented as mean ± SEM. $*p < 0.05$, $**p < 0.01$, and $***p < 0.001$. Abbreviations: NG, normoglycemic culture conditions; HG, hyperglycemic culture conditions; PA, palmitic acid; HG+PA, hyperglycemic culture conditions supplemented with PA to mimic T2DM at the cellular level; OE, overexpression; NC, negative control with blank plasmid; siNC, scramble negative control construct for siRNAs; siRPS5, siRNA targeting RPS5; siMRPS5, siRNA targeting MRPS5.

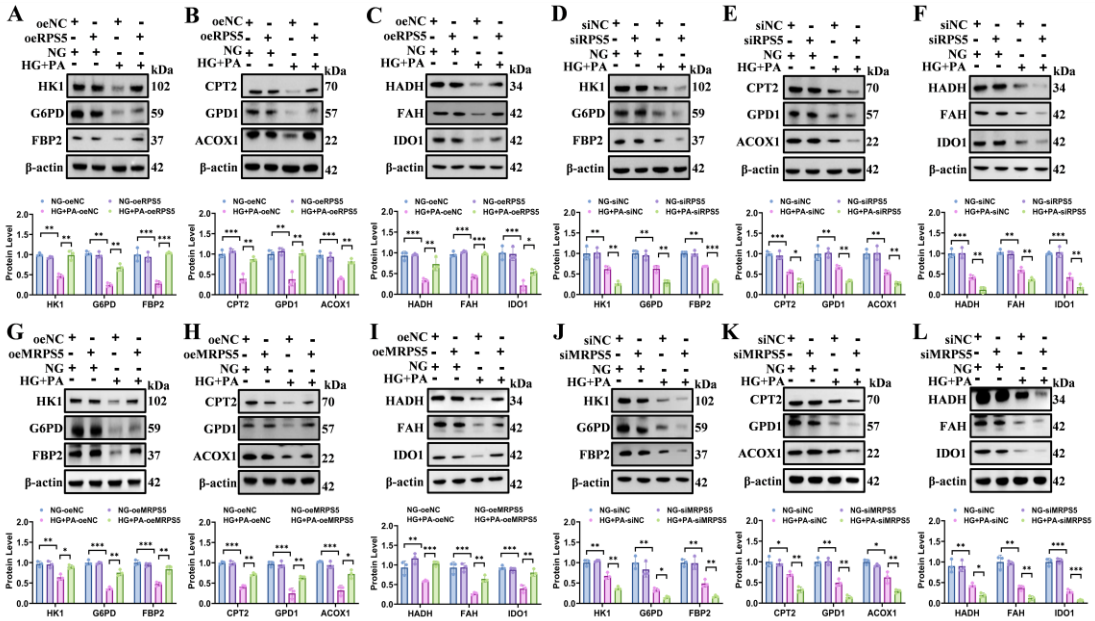

Figure 6. RPS5–MRPS5 translational capacity governs metabolic enzyme abundance across cardiac fuel pathways. The RPS5–MRPS5 axis controls the abundance of enzymes required for glucose, lipid, and amino acid metabolism, linking translational capacity to metabolic network output. **(A)** Representative immunoblot analysis of key enzymes involved in glucose metabolism, including glycolytic, pentose phosphate pathway, and pyruvate oxidation components, in cardiomyocytes under control and diabetic conditions, and following RPS5 overexpression (n = 3). β-actin was used as a loading control. The bottom panel: Quantification of glucose metabolism related protein expression. **(B)** Representative immunoblot analysis of lipid metabolism–associated enzymes, including regulators of mitochondrial β-oxidation and peroxisomal fatty acid oxidation, in cardiomyocytes under control and diabetic conditions, and following RPS5 overexpression (n = 3). β-actin was used as a loading control. The bottom panel: Quantification of lipid metabolism related protein expression. **(C)** Representative immunoblot analysis of amino acid metabolism–related enzymes, including components linked to TCA cycle anaplerosis, redox balance, and detoxification pathways, following HG+PA exposure and RPS5 overexpression (n = 3). β-actin was used as a loading control. The bottom panel: Quantification of amino acid metabolism related protein expression. **(D)** Representative immunoblot analysis of key enzymes involved in glucose metabolism, including glycolytic, pentose phosphate pathway, and pyruvate oxidation components, in cardiomyocytes under control and diabetic conditions and following knockdown of RPS5 expression (n = 3). β-actin was used as a loading control. The bottom panel: Quantification of glucose metabolism related protein expression. **(E)** Representative immunoblot analysis of lipid metabolism–associated enzymes, including regulators of mitochondrial β-oxidation and peroxisomal fatty acid oxidation, in cardiomyocytes under control and diabetic conditions, and knockdown of RPS5 expression (n = 3). The bottom panel: Quantification of lipid metabolism related protein expression. **(F)** Representative immunoblot analysis of amino acid metabolism–related enzymes, including components linked to TCA cycle anaplerosis, redox balance, and detoxification pathways, following HG+PA exposure and knockdown of RPS5 expression (n = 3). **(G)** Representative immunoblot analysis of key enzymes involved in glucose metabolism, including glycolytic, pentose phosphate pathway, and pyruvate oxidation components,

in cardiomyocytes under control and diabetic conditions, and following MRPS5 overexpression (n = 3). β-actin was used as a loading control. The bottom panel: Quantification of glucose metabolism related protein expression. **(H)** Representative immunoblot analysis of lipid metabolism–associated enzymes, including regulators of mitochondrial β-oxidation and peroxisomal fatty acid oxidation, in cardiomyocytes under control conditions, HG+PA treatment, and following MRPS5 overexpression (n = 3). β-actin was used as a loading control. The bottom panel: Quantification of lipid metabolism related protein expression. **(I)** Representative immunoblot analysis of amino acid metabolism–related enzymes, including components linked to TCA cycle anaplerosis, redox balance, and detoxification pathways, following HG+PA exposure and MRPS5 overexpression (n = 3). β-actin was used as a loading control. The bottom panel: Quantification of amino acid metabolism related protein expression. **(J)** Representative immunoblot analysis of key enzymes involved in glucose metabolism, including glycolytic, pentose phosphate pathway, and pyruvate oxidation components, in cardiomyocytes under control and diabetic conditions, and following knockdown of MRPS5 expression (n = 3). β-actin was used as a loading control. The bottom panel: Quantification of glucose metabolism related protein expression. **(K)** Representative immunoblot analysis of lipid metabolism–associated enzymes, including regulators of mitochondrial β-oxidation and peroxisomal fatty acid oxidation, in cardiomyocytes under control and diabetic conditions, and knockdown of MRPS5 expression (n = 3). β-actin was used as a loading control. The bottom panel: Quantification of lipid metabolism related protein expression. **(L)** Representative immunoblot analysis of amino acid metabolism–related enzymes, including components linked to TCA cycle anaplerosis, redox balance, and detoxification pathways, following HG+PA exposure and knockdown of MRPS5 expression (n = 3). β-actin was used as a loading control. The bottom panel: Quantification of amino acid metabolism related protein expression. Statistical significance was determined using the tests described in the Methods. All data are presented as mean ± SEM. *$p < 0.05$, **$p < 0.01$, and ***$p < 0.001$.

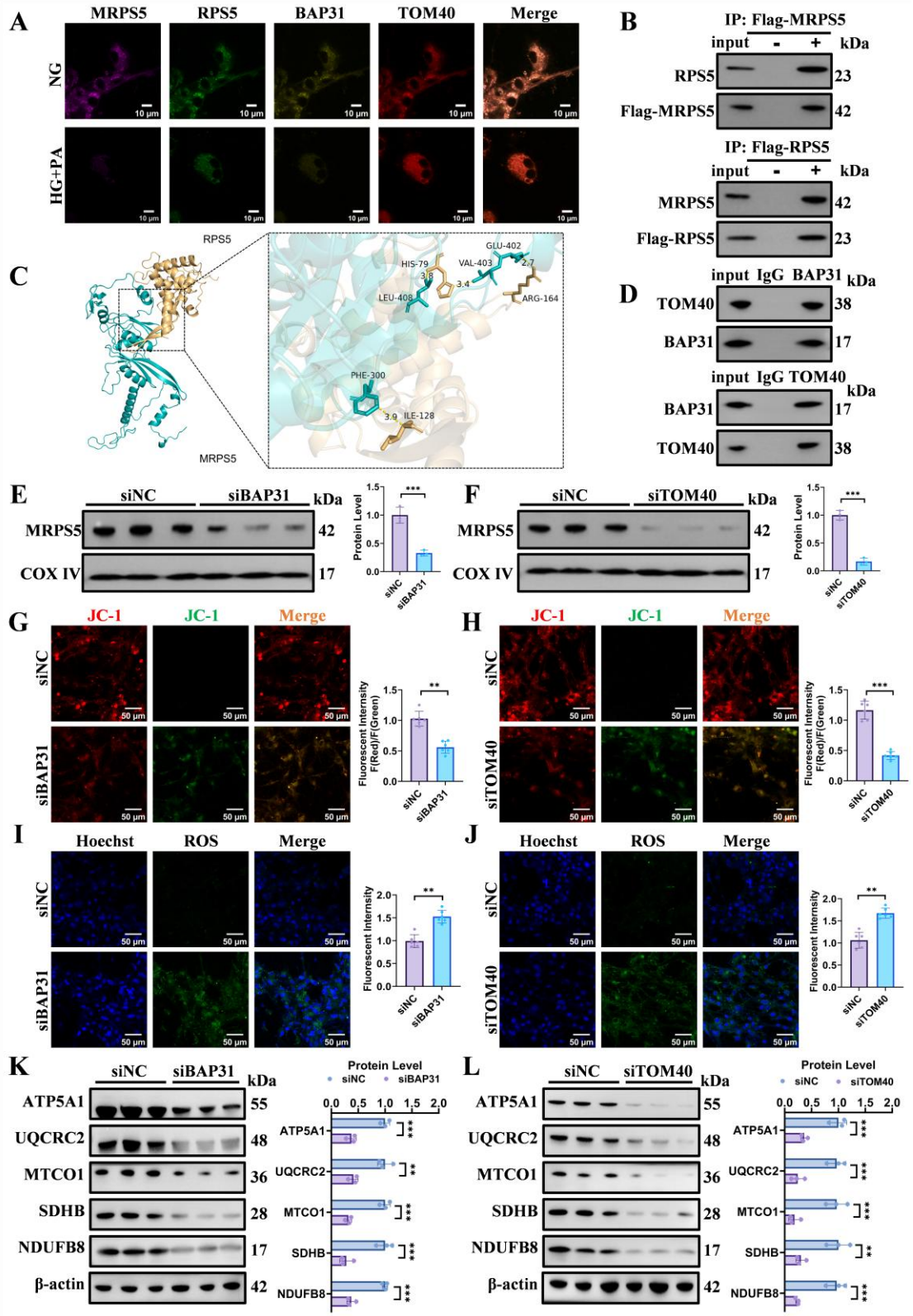

Figure 7. BAP31 and TOMM40 mediate RPS5–MRPS5 coupling at ER–mitochondria contact sites. ER–mitochondria contact site components BAP31 and TOMM40 mediate the physical and functional coupling between cytosolic RPS5 and mitochondrial MRPS5. **(A)** Representative confocal immunofluorescence images showing the colocalization of MRPS5 (purple), RPS5 (green), BAP31 (yellow), and TOMM40 (red) in cardiomyocytes cultured under normal glucose or high glucose plus

palmitic acid conditions (n = 6). Scale bar: 10 μm. **(B)** Co-immunoprecipitation (Co-IP) analysis of endogenous RPS5 and MRPS5 from cardiomyocyte lysates (n = 3). **(C)** Structural model of the RPS5–MRPS5 complex generated by AlphaFold-based docking. The overall predicted interaction interface between RPS5 and MRPS5 is shown on the left. A magnified view on the right highlights key interacting residues, including RPS5 Arg-164 and MRPS5 Glu-402, as well as surrounding stabilizing contacts, providing a structural basis for the experimentally observed interaction. **(D)** Co-immunoprecipitation (Co-IP) analysis of endogenous BAP31 and TOMM40 from cardiomyocyte lysates (n = 3). **(E)** Western blot analysis of mitochondrial MRPS5 protein levels in cardiomyocytes transfected with control siRNA or BAP31-specific siRNA. Knockdown of BAP31 significantly reduced MRPS5 expression within the mitochondrial fraction (n = 3). COX IV was used as a mitochondrial loading control. The right panel shows the quantification of protein expression levels. **(F)** Western blot analysis of mitochondrial MRPS5 protein levels in cardiomyocytes transfected with control siRNA or TOMM40-specific siRNA. Knockdown of TOMM40 significantly reduced MRPS5 expression within the mitochondrial fraction (n = 3). COX IV was used as a mitochondrial loading control. The right panel shows the quantification of protein expression levels. **(G)** Assessment of mitochondrial membrane potential (ΔΨm) by JC-1 staining in cardiomyocytes with or without BAP31 knockdown. Representative immunofluorescence images are shown. Scale bars, 50 μm. Quantification of the JC-1 red/green ratio is presented in the right panel (n = 6). **(H)** Assessment of mitochondrial membrane potential (ΔΨm) by JC-1 staining in cardiomyocytes with or without TOM40 knockdown. Representative immunofluorescence images are shown. Scale bars, 50 μm. Quantification of the JC-1 red/green ratio is presented in the right panel (n = 6). **(I)** Measurement of cellular reactive oxygen species (ROS) levels using DCF fluorescence in cardiomyocytes with or without BAP31 knockdown. Representative immunofluorescence images are shown. Scale bars, 50 μm. Quantitative analysis of relative fluorescence intensity in the right panel (n = 6). **(J)** Measurement of cellular reactive oxygen species (ROS) levels using DCF fluorescence in cardiomyocytes with or without TOM40 knockdown. Representative immunofluorescence images are shown. Scale bars, 50 μm. Quantitative analysis of relative fluorescence intensity in the right panel (n = 6). **(K)** Representative Western blot analysis of oxidative phosphorylation (OXPHOS) complex subunits, including NDUFB8 (Complex I), SDHB (Complex II), UQCRC2 (Complex III), and ATP5A (Complex V), in cardiomyocytes with or without BAP31 knockdown (n = 3). β-actin served as a loading control. The right panel shows the quantification of protein expression levels. **(L)** Representative Western blot analysis of OXPHOS complex subunits, including NDUFB8 (Complex I), SDHB (Complex II), UQCRC2 (Complex III), and ATP5A (Complex V), in cardiomyocytes with or without TOM40 knockdown (n = 3). β-actin served as a loading control. The right panel shows the quantification of protein expression levels. Statistical significance was determined using the tests described in the Methods. All data are presented as mean ± SEM. *p < 0.05, **p < 0.01, and ***p < 0.001.

Supplementary Figures

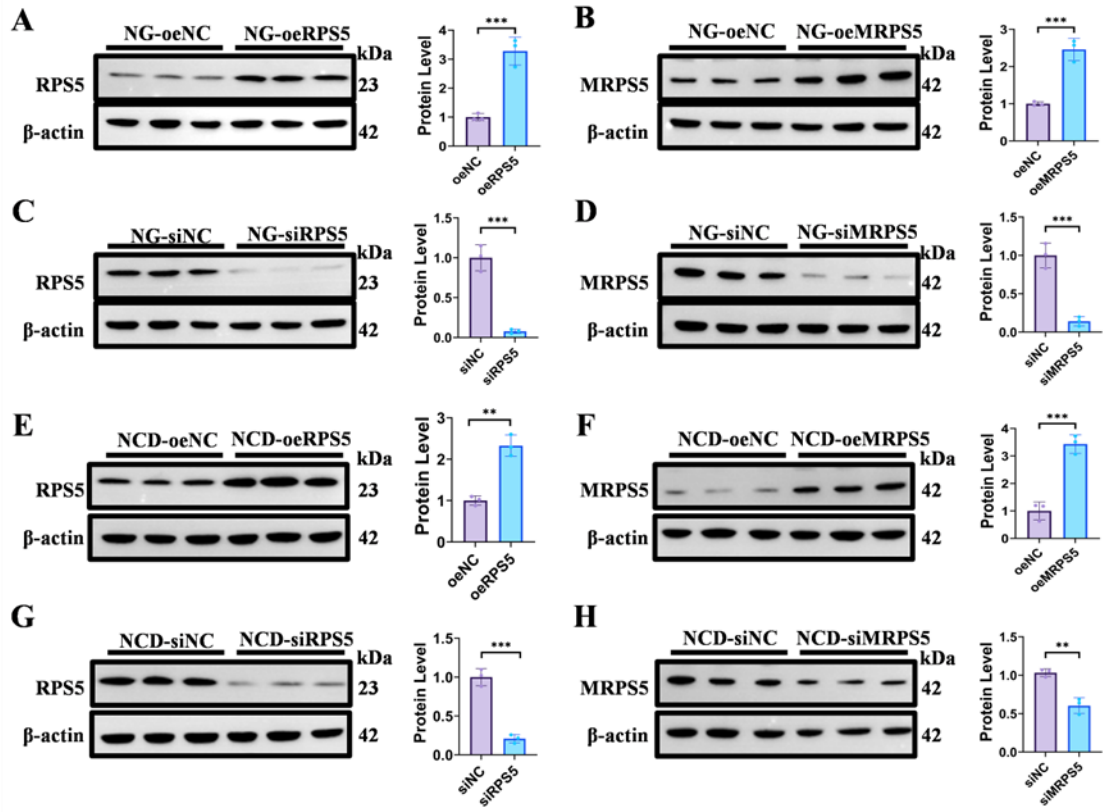

Figure S1. Efficient manipulation of RPS5 and MRPS5 expression in vitro and in vivo. Overexpression and knockdown strategies robustly modulate RPS5 and MRPS5 protein levels in cardiomyocytes and mouse hearts. **(A–B)** Representative immunoblot analyses confirming overexpression of RPS5 (oeRPS5; **A**) and MRPS5 (oeMRPS5; **B**) in cardiomyocytes under normoglycemic (NG) conditions. β-actin serves as a loading control. Right panels: quantification of protein expression levels (n = 3 independent biological replicates). **(C–D)** Representative immunoblot analyses validating siRNA-mediated knockdown of RPS5 (siRPS5; **C**) and MRPS5 (siMRPS5; **D**) in cardiomyocytes under NG conditions. β-actin serves as a loading control. Right panels: quantification of protein expression levels (n = 3). **(E–F)** Representative immunoblot analyses confirming AAV9-mediated cardiomyocyte-specific overexpression of RPS5 (oeRPS5; **E**) and MRPS5 (oeMRPS5; **F**) in mouse hearts under normal chow diet (NCD) conditions. β-actin serves as a loading control. Right panels: quantification of protein expression levels (n = 3). **(G–H)** Representative immunoblot analyses validating cardiac-specific knockdown of RPS5 (siRPS5; **G**) and MRPS5 (siMRPS5; **H**) in mouse hearts under NCD conditions. β-actin serves as a loading control. Right panels: quantification of protein expression levels (n = 3). Data are presented as mean ± SEM. Statistical significance was determined as described in Methods. $^{**}P < 0.01$, $^{***}P < 0.001$. Abbreviations: NG, normoglycemic conditions; NCD, normal chow diet; oeNC, empty vector control; oeRPS5, RPS5 overexpression; oeMRPS5, MRPS5 overexpression; siNC, scramble control; siRPS5, RPS5-targeting siRNA; siMRPS5, MRPS5-targeting siRNA.

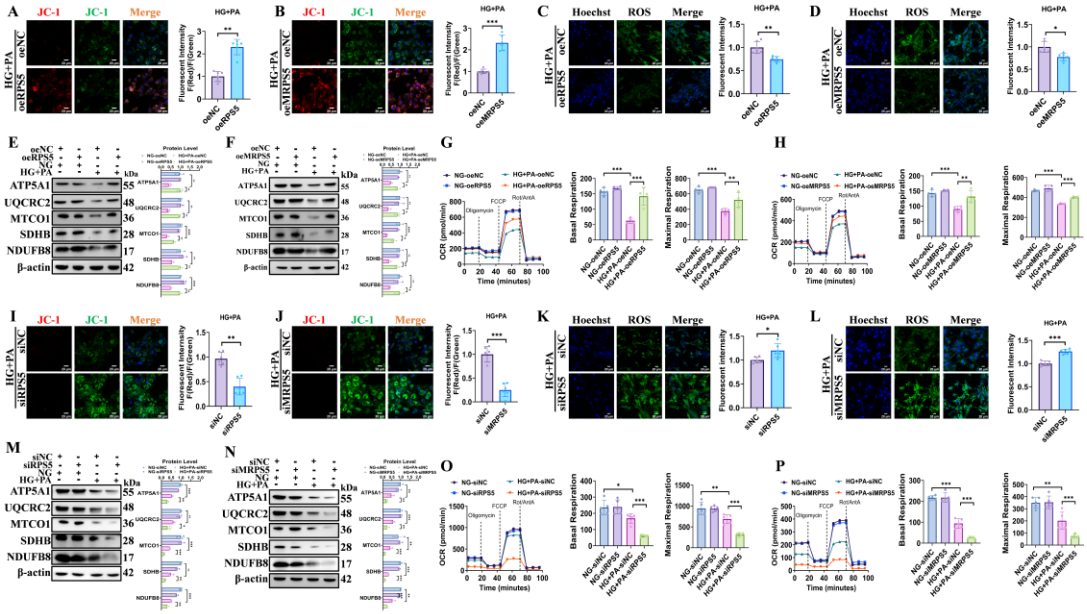

Figure S2. RPS5–MRPS5 axis preserves mitochondrial function and limits oxidative stress under diabetic conditions. (A) Assessment of mitochondrial membrane potential (ΔΨm) by JC-1 staining in cardiomyocytes under control or diabetic conditions with or without RPS5 overexpression. Representative immunofluorescence images are shown. HG + PA treatment induced mitochondrial depolarization, as evidenced by a reduced JC-1 red/green fluorescence ratio, which was significantly attenuated by RPS5 overexpression. Scale bars, 20 μm. Right panel: quantification of the JC-1 red/green ratio (n = 6). **(B)** Assessment of mitochondrial membrane potential (ΔΨm) by JC-1 staining in cardiomyocytes under control or diabetic conditions with or without MRPS5 overexpression. Representative immunofluorescence images are shown. HG + PA treatment induced mitochondrial depolarization, which was significantly attenuated by MRPS5 overexpression. Scale bars, 20 μm. Right panel: quantification of the JC-1 red/green ratio (n = 6). **(C)** Measurement of cellular reactive oxygen species (ROS) levels using DCF fluorescence in cardiomyocytes under control or diabetic conditions with or without RPS5 overexpression. Scale bars, 20 μm. Right panel: quantitative analysis of relative fluorescence intensity, indicating that HG+PA-induced ROS elevation was markedly reduced upon RPS5 overexpression (n = 6). **(D)** Measurement of cellular reactive oxygen species (ROS) levels using DCF fluorescence in cardiomyocytes under control or diabetic conditions with or without MRPS5 overexpression. Scale bars, 20 μm. Right panel: quantitative analysis of relative fluorescence intensity, indicating that HG + PA-induced ROS elevation was markedly reduced upon MRPS5 overexpression (n = 6). **(E)** Representative Western blot analysis of oxidative phosphorylation (OXPHOS) complex subunits, including NDUFB8 (Complex I), SDHB (Complex II), UQCRC2 (Complex III), and ATP5A (Complex V), in cardiomyocytes under control or diabetic conditions with or without RPS5 overexpression. β-actin served as a loading control (n = 3). Right panel: quantification of protein expression levels. HG + PA-induced suppression of OXPHOS subunits was restored by RPS5 overexpression. **(F)** Representative Western blot analysis of OXPHOS complex subunits, including NDUFB8 (Complex I), SDHB (Complex II), UQCRC2 (Complex III), and ATP5A (Complex V), in cardiomyocytes under control or diabetic conditions with or without MRPS5 overexpression. β-actin served as a loading control (n = 3). Right panel: quantification of protein expression levels. HG + PA-induced suppression of OXPHOS

subunits was restored by MRPS5 overexpression. **(G)** Mitochondrial respiratory function assessed by Seahorse extracellular flux analysis in cardiomyocytes under control or diabetic conditions with or without RPS5 overexpression. Oxygen consumption rate (OCR) was measured over time following sequential injections of oligomycin, FCCP, and rotenone/antimycin A. Right panels: quantification of basal and maximal respiration rates. HG+PA treatment impaired mitochondrial respiration, whereas RPS5 overexpression significantly enhanced both basal and maximal OCR compared with HG+PA controls (n = 4). **(H)** Mitochondrial respiratory function assessed by Seahorse extracellular flux analysis in cardiomyocytes under control or diabetic conditions with or without MRPS5 overexpression. Oxygen consumption rate (OCR) was measured over time following sequential injections of oligomycin, FCCP, and rotenone/antimycin A. Right panels: quantification of basal and maximal respiration rates. HG + PA treatment impaired mitochondrial respiration, whereas MRPS5 overexpression significantly enhanced both basal and maximal OCR compared with HG + PA controls (n = 4). Statistical significance was determined using the tests described in the Methods. NG, normoglycemic culture conditions; HG, hyperglycemic culture conditions; PA, palmitic acid; HG+PA, hyperglycemic culture conditions supplemented with PA to mimic T2DM at the cellular level; OE, overexpression. **(I)** Assessment of mitochondrial membrane potential (ΔΨm) by JC-1 staining in cardiomyocytes under high-glucose and high-palmitic acid conditions with or without RPS5 knockdown. Representative immunofluorescence images are shown. HG+PA treatment induced mitochondrial depolarization, as evidenced by a reduced JC-1 red/green fluorescence ratio, which was further exacerbated by RPS5 knockdown (n = 6). Scale bars, 20 μm. Quantification of the JC-1 red/green ratio is presented in the right panel. **(J)** Assessment of mitochondrial membrane potential (ΔΨm) by JC-1 staining in cardiomyocytes under HG+PA conditions with or without MRPS5 knockdown. Representative immunofluorescence images are shown. HG+PA treatment induced mitochondrial depolarization, as evidenced by a reduced JC-1 red/green fluorescence ratio, which was further exacerbated by MRPS5 knockdown. Scale bars, 20 μm. Quantification of the JC-1 red/green ratio is presented in the right panel (n = 6). **(K)** Measurement of cellular reactive oxygen species (ROS) levels using DCF fluorescence in cardiomyocytes under HG+PA conditions with or without RPS5 knockdown. The right panel shows the quantitative analysis of relative fluorescence intensity, indicating that HG+PA-induced ROS elevation was markedly increased upon RPS5 knockdown (n = 6). Scale bars, 20 μm. **(L)** Measurement of cellular reactive oxygen species (ROS) levels using DCF fluorescence in cardiomyocytes under HG+PA conditions with or without MRPS5 knockdown. The right panel shows the quantitative analysis of relative fluorescence intensity, indicating that HG+PA-induced ROS elevation was markedly increased upon RPS5 knockdown (n = 6 independent biological replicates). Scale bars, 20 μm. **(M)** Representative Western blot analysis of OXPHOS complex subunits, including NDUFB8 (Complex I), SDHB (Complex II), UQCRC2 (Complex III), and ATP5A (Complex V), in cardiomyocytes under NG or HG+PA conditions with or without RPS5 knockdown (n = 3). β-actin served as a loading control. The right panel shows the quantification of protein expression levels. HG+PA-induced suppression of OXPHOS subunits was further exacerbated by RPS5 knockdown. **(N)** Representative Western blot analysis of OXPHOS complex subunits, including NDUFB8 (Complex I), SDHB (Complex II), UQCRC2 (Complex III), and ATP5A (Complex V), in cardiomyocytes under NG or HG+PA conditions with or without MRPS5 knockdown (n = 3). β-actin served as a loading control. The right panel shows the quantification of protein expression levels. HG+PA-induced suppression of OXPHOS subunits was

further exacerbated by MRPS5 knockdown. **(O)** Mitochondrial respiratory function assessed by Seahorse extracellular flux analysis in cardiomyocytes under NG or HG+PA conditions with or without RPS5 knockdown. Oxygen consumption rate (OCR) was measured over time following sequential injections of oligomycin, FCCP, and rotenone/antimycin A. The right panels show the quantification of basal and maximal respiration rates. HG+PA treatment impaired mitochondrial respiration, and RPS5 knockdown further suppressed both basal and maximal OCR compared to HG+PA controls (n = 4). **(P)** Mitochondrial respiratory function assessed by Seahorse extracellular flux analysis in cardiomyocytes under NG or HG+PA conditions with or without MRPS5 knockdown. Oxygen consumption rate (OCR) was measured over time following sequential injections of oligomycin, FCCP, and rotenone/antimycin A. The right panels show the quantification of basal and maximal respiration rates. HG+PA treatment impaired mitochondrial respiration, and MRPS5 knockdown further suppressed both basal and maximal OCR compared to HG+PA controls (n = 4). Statistical significance was determined using the tests described in the Methods. All data are presented as mean ± SEM. *$p < 0.05$, **$p < 0.01$, and ***$p < 0.001$.

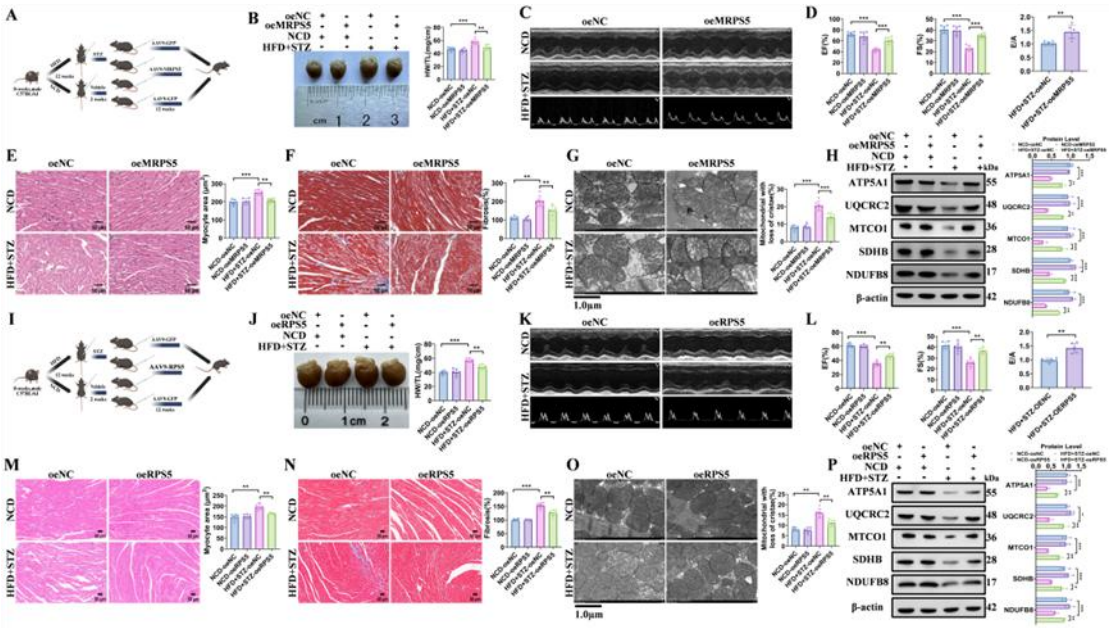

Figure S3. Cardiac-specific restoration of RPS5 or MRPS5 rescues cardiac function and mitochondrial integrity in diabetic cardiomyopathy in vivo. Cardiac-specific restoration of RPS5 or MRPS5 reverses structural remodeling, improves contractile function, and preserves mitochondrial integrity in diabetic cardiomyopathy in vivo. **(A)** Schematic illustration of the experimental design for cardiac-specific manipulation of MRPS5 in a mouse model of diabetic cardiomyopathy (DCM). Diabetic mice received AAV9-mediated cardiomyocyte-specific MRPS5 overexpression or control vectors (n = 6). **(B)** Left panel: gross morphology of excised hearts from each experimental group (n = 6), demonstrating attenuation of cardiac hypertrophy following MRPS5 overexpression. Right panel: quantification of heart weight–to–tibia length ratio, indicating reduced pathological cardiac remodeling in MRPS5-treated DCM mice. **(C)** Representative M-mode echocardiographic images and Doppler tracings illustrating left ventricular systolic and diastolic function in control, DCM, and MRPS5-treated DCM mice (n = 6). **(D)** Quantitative echocardiographic assessment of cardiac function, including ejection fraction (EF), fractional shortening (FS), and E/A ratio (n = 6). MRPS5 overexpression significantly improves both systolic and diastolic performance in DCM hearts. **(E)** Left panels: representative hematoxylin–eosin (H&E)-stained cardiac sections showing myocardial architecture across experimental groups (n = 6). Scale bars, 50 μm. Right panel: quantification of myocyte area. **(F)** Left panels: representative Masson's trichrome-stained cardiac sections illustrating interstitial and perivascular fibrosis (n = 6). Scale bars, 50 μm. Right panel: quantification of myocardial fibrosis area. MRPS5 overexpression markedly reduces collagen deposition. **(G)** Left panels: representative transmission electron microscopy (TEM) images of cardiac mitochondria (n = 6). Scale bars, 1 μm. DCM hearts exhibit swollen, structurally disrupted mitochondria, whereas MRPS5 overexpression preserves mitochondrial ultrastructure. Right panel: quantification of mitochondrial cristae. **(H)** Representative Western blot analysis of oxidative phosphorylation (OXPHOS) complex subunits, including NDUFB8 (Complex I), SDHB (Complex II), UQCRC2 (Complex III), and ATP5A (Complex V), in heart tissues from control, DCM, and DCM mice with MRPS5 overexpression (n = 3). β-actin served as a loading control. Right panel: quantification of protein expression levels. Suppression of OXPHOS subunits in DCM hearts was restored by MRPS5

overexpression. **(I)** Schematic illustration of the experimental design for cardiac-specific overexpression of RPS5 in a mouse model of DCM. Diabetic mice received AAV9-mediated cardiomyocyte-specific RPS5 overexpression or control vectors (n = 6). **(J)** Left panel: gross morphology of excised hearts from each experimental group (n = 6), demonstrating attenuation of cardiac hypertrophy following RPS5 overexpression. Right panel: quantification of heart weight–to–tibia length ratio, indicating reduced pathological cardiac remodeling in RPS5-treated DCM mice. **(K)** Representative M-mode echocardiographic images and Doppler tracings illustrating left ventricular systolic and diastolic function in control, DCM, and RPS5-treated DCM mice (n = 6). **(L)** Quantitative echocardiographic assessment of cardiac function, including ejection fraction (EF), fractional shortening (FS), and E/A ratio (n = 6). RPS5 overexpression significantly improves both systolic and diastolic performance in DCM hearts. **(M)** Left panels: representative hematoxylin–eosin (H&E)-stained cardiac sections showing myocardial architecture across experimental groups (n = 6). Scale bars, 50 μm. Right panel: quantification of myocyte cross-sectional area. **(N)** Left panels: representative Masson's trichrome-stained cardiac sections illustrating interstitial and perivascular fibrosis (n = 6). Scale bars, 50 μm. Right panel: quantification of myocardial fibrosis area. RPS5 overexpression markedly reduces collagen deposition. **(O)** Left panels: representative transmission electron microscopy (TEM) images of cardiac mitochondria (n = 6). Scale bars, 1 μm. DCM hearts exhibit swollen, structurally disrupted mitochondria, whereas RPS5 overexpression preserves mitochondrial ultrastructure. Right panel: quantification of mitochondrial cristae density. **(P)** Representative Western blot analysis of OXPHOS complex subunits, including ATP5A (Complex V), UQCRC2 (Complex III), MTCO1 (Complex IV), SDHB (Complex II), and NDUFB8 (Complex I), in heart tissues from control, DCM, and DCM mice with RPS5 overexpression (n = 3). β-actin served as a loading control. Right panel: quantification of protein expression levels, demonstrating restoration of mitochondrial respiratory protein expression in RPS5-treated DCM hearts. All data are presented as mean ± SEM. *$p < 0.05$, **$p < 0.01$, and ***$p < 0.001$.

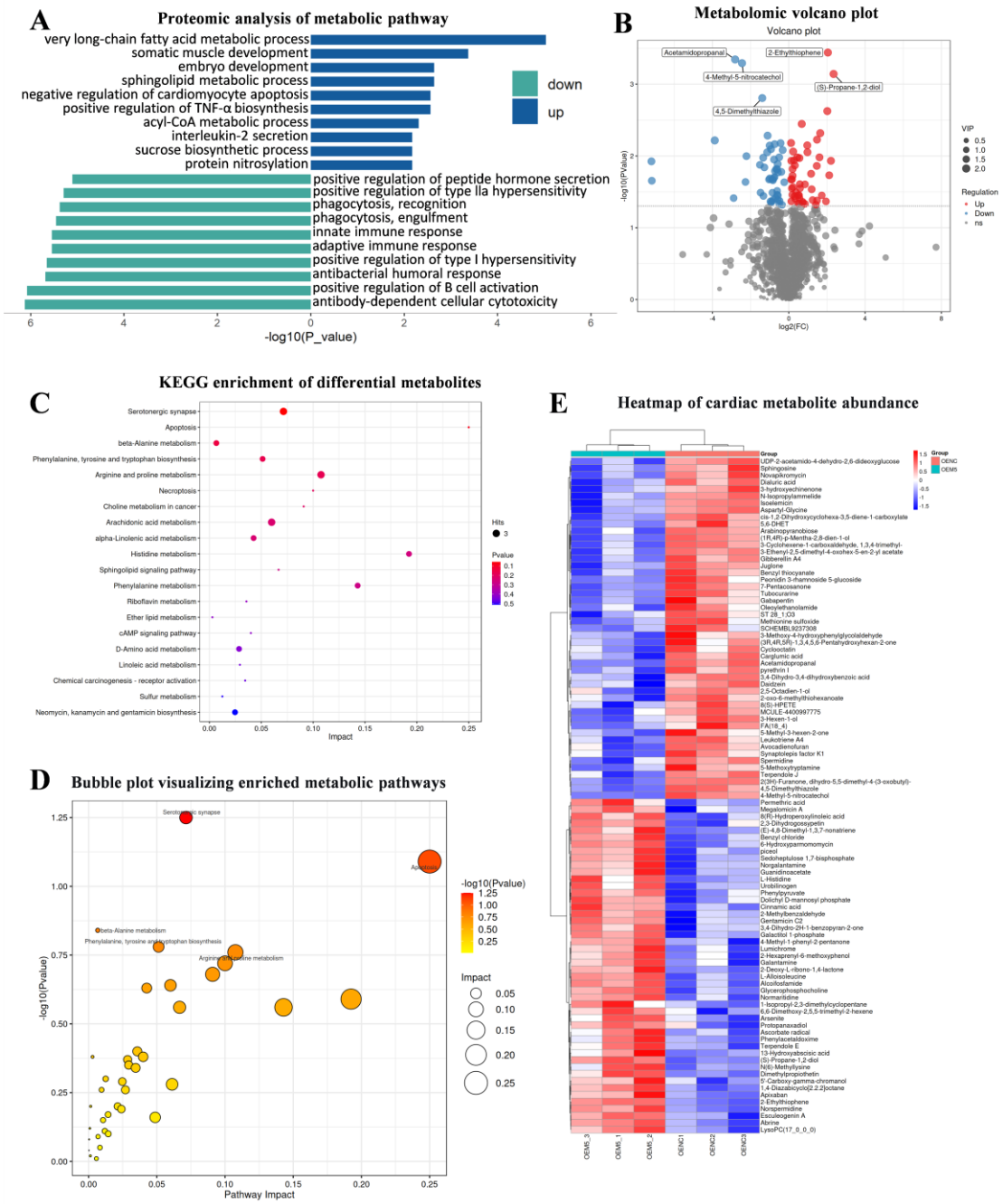

Figure S4. Restoration of translational capacity normalizes cardiac metabolic profiles in vivo. MRPS5 restoration broadly reprograms metabolic pathways and metabolite profiles, indicating recovery of cardiac metabolic homeostasis in vivo. **(A)** Proteomic analysis revealed that MRPS5 overexpression restored multiple metabolic pathways in DCM hearts (n = 3). Compared with control hearts, metabolic pathways including long-chain fatty acid metabolic process and tricarboxylic acid cycle were downregulated in DCM hearts and significantly upregulated upon MRPS5 overexpression. **(B)** Metabolomic analysis demonstrated that MRPS5 overexpression corrected DCM-associated metabolic disturbances. Volcano plot depicting the overall distribution of differential metabolites between MRPS5-overexpressing diabetic and diabetic control heart tissues. Red dots represent significantly upregulated metabolites following MRPS5 treatment, while blue dots indicate downregulated metabolites.

Numerous metabolic intermediates with aberrant levels in DCM hearts were restored upon MRPS5 overexpression. **(C)** KEGG pathway enrichment analysis of differential metabolites in the hearts of MRPS5-overexpressing diabetic mice versus untreated diabetic controls. The analysis revealed significant enrichment of multiple metabolic pathways. **(D)** Bubble plot depicting the enriched metabolic pathways. The Rich factor represents the ratio of differential metabolites to total metabolites annotated within each pathway, with bubble color indicating the significance level (P value) and bubble size representing the impact score of enrichment. **(E)** Heatmap showing the relative abundance of representative cardiac metabolites across experimental groups. Data are presented as normalized values, with red indicating higher abundance and blue indicating lower abundance.

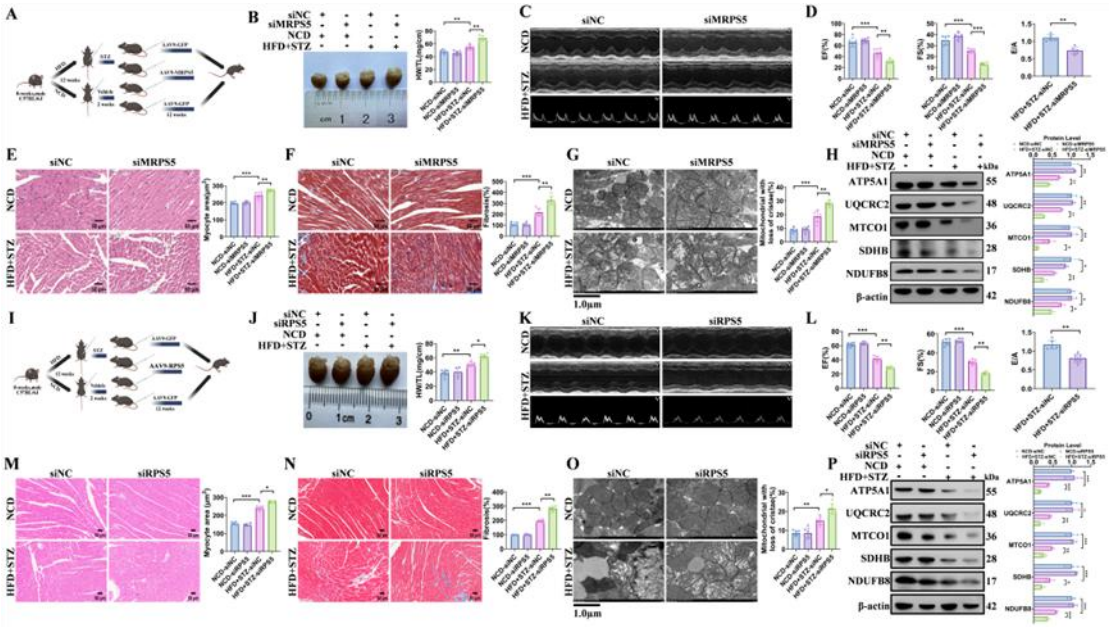

Figure S5. Cardiac-specific RPS5 or MRPS5 knockdown alone exacerbates cardiac structural, functional, and metabolic disorders in diabetic cardiomyopathy in vivo. (A) Schematic illustration of the experimental design for cardiac-specific knockdown of MRPS5 in a mouse model of diabetic cardiomyopathy (DCM). Diabetic mice received AAV9-mediated cardiomyocyte-specific MRPS5 knockdown or control vectors (n = 6). **(B)** Left panel: Gross morphology of excised hearts from each experimental group (n = 6), demonstrating exacerbated cardiac hypertrophy following MRPS5 knockdown. Right panel: Quantification of heart weight–to–tibia length ratio, indicating aggravated pathological cardiac remodeling in MRPS5-deficient DCM mice. **(C)** Representative M-mode echocardiographic images and Doppler tracings illustrating left ventricular systolic and diastolic function in control, DCM, and MRPS5-knockdown DCM mice (n = 6). **(D)** Quantitative echocardiographic assessment of cardiac function, including ejection fraction (EF), fractional shortening (FS), and E/A ratio (n = 6). MRPS5 knockdown significantly exacerbates both systolic and diastolic dysfunction in DCM hearts. **(E)** Left panels: Representative hematoxylin–eosin (H&E)–stained cardiac sections showing myocardial architecture across experimental groups (n = 6 mice per group). Scale bars, 50 μm. Right panel: Quantification of myocyte cross-sectional area, revealing aggravated cardiomyocyte hypertrophy upon MRPS5 knockdown. **(F)** Left panels: Representative Masson's trichrome–stained cardiac sections illustrating interstitial and perivascular fibrosis (n = 6). MRPS5 knockdown markedly increases collagen deposition. Scale bars, 50 μm. Right panel: Quantification of myocardial fibrosis area derived from Masson's trichrome staining. **(G)** Left panels: Representative transmission electron microscopy (TEM) images of cardiac mitochondria (n = 6). DCM hearts exhibit swollen, structurally disrupted mitochondria, and MRPS5 knockdown further exacerbates mitochondrial ultrastructural damage. Scale bars, 1 μm. Right panel: Quantification of mitochondrial cristae density. **(H)** Representative Western blot analysis of oxidative phosphorylation (OXPHOS) complex subunits, including NDUFB8 (Complex I), SDHB (Complex II), UQCRC2 (Complex III), and ATP5A (Complex V), in heart tissues from control, diabetic (DCM), and DCM mice with MRPS5 knockdown (n = 3). β-actin served as a loading control. The right panel shows the quantification of protein expression levels. The suppression of OXPHOS subunits

observed in DCM hearts was further exacerbated by MRPS5 knockdown. **(I)** Schematic illustration of the experimental design for cardiac-specific knockdown of RPS5 in a mouse model of DCM. Diabetic mice received AAV9-mediated cardiomyocyte-specific RPS5 knockdown or control vectors (n = 6). **(J)** Left panel: gross morphology of excised hearts from each experimental group (n = 6), demonstrating aggravated cardiac hypertrophy following RPS5 knockdown. Right panel: quantification of heart weight–to–tibia length ratio, indicating enhanced pathological cardiac remodeling in RPS5-deficient DCM mice. **(K)** Representative M-mode echocardiographic images and Doppler tracings illustrating left ventricular systolic and diastolic function in control, DCM, and RPS5-knockdown DCM mice (n = 6). **(L)** Quantitative echocardiographic assessment of cardiac function, including ejection fraction (EF), fractional shortening (FS), and E/A ratio (n = 6). RPS5 knockdown significantly exacerbates both systolic and diastolic dysfunction in DCM hearts. **(M)** Left panels: representative hematoxylin–eosin (H&E)-stained cardiac sections showing myocardial architecture across experimental groups (n = 6). Scale bars, 50 μm. Right panel: quantification of myocyte cross-sectional area, revealing aggravated cardiomyocyte hypertrophy upon RPS5 knockdown. **(N)** Left panels: representative Masson's trichrome-stained cardiac sections illustrating interstitial and perivascular fibrosis (n = 6). Scale bars, 50 μm. Right panel: quantification of myocardial fibrosis area. RPS5 knockdown markedly increases collagen deposition. **(O)** Left panels: representative transmission electron microscopy (TEM) images of cardiac mitochondria (n = 6). Scale bars, 1 μm. DCM hearts exhibit swollen, structurally disrupted mitochondria, and RPS5 knockdown further exacerbates mitochondrial ultrastructural damage. Right panel: quantification of mitochondrial cristae density. **(P)** Representative Western blot analysis of OXPHOS complex subunits, including ATP5A (Complex V), UQCRC2 (Complex III), MTCO1 (Complex IV), SDHB (Complex II), and NDUFB8 (Complex I), in heart tissues from control, DCM, and DCM mice with RPS5 knockdown (n = 3). β-actin served as a loading control. Right panel: quantification of protein expression levels, demonstrating further suppression of mitochondrial respiratory proteins in RPS5-deficient DCM hearts. Statistical significance was determined using the tests described in the Methods. All data are presented as mean ± SEM. *$p < 0.05$, **$p < 0.01$, and ***$p < 0.001$.

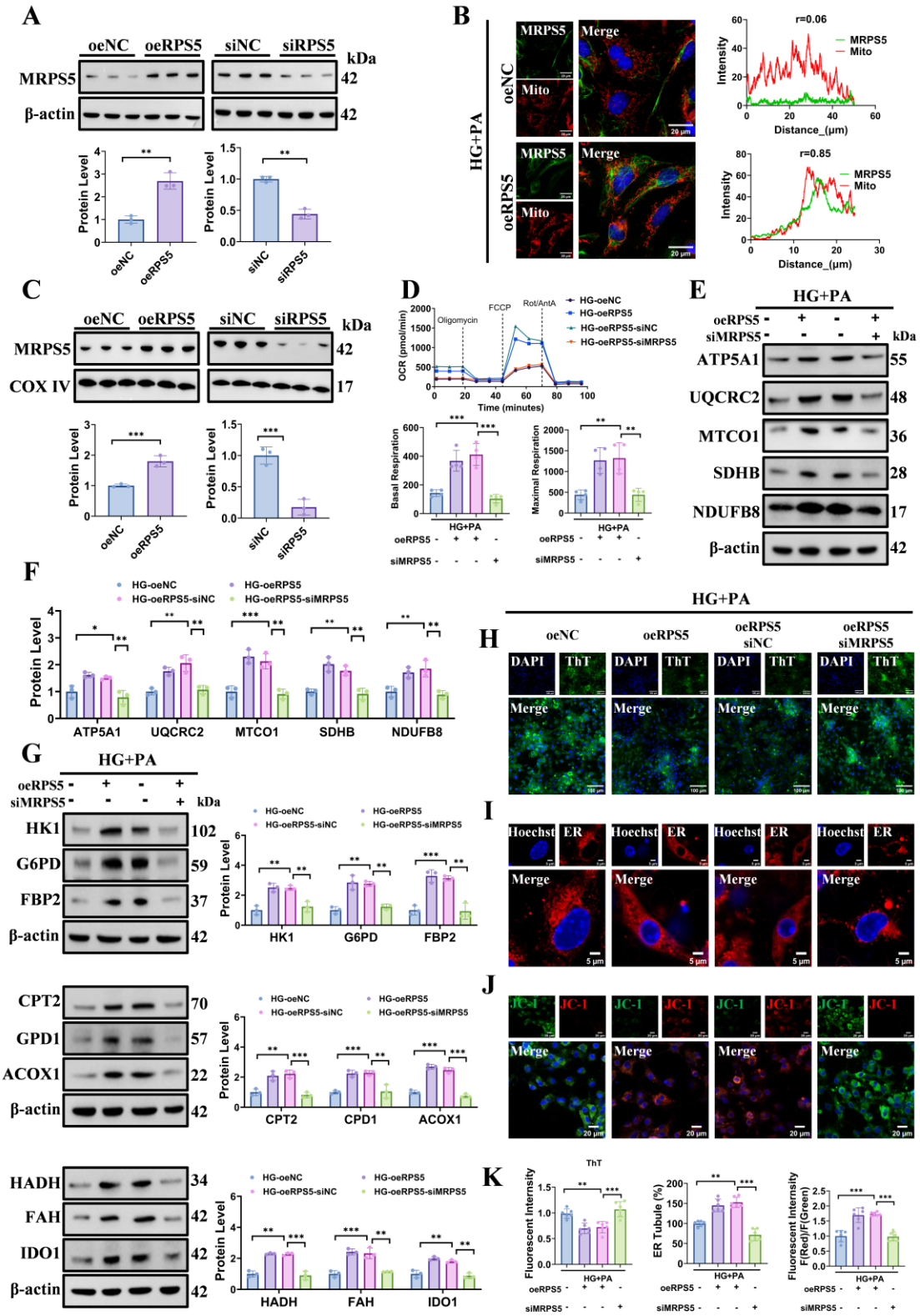

Figure S6. RPS5 controls MRPS5 expression, mitochondrial targeting, and downstream metabolic and proteostatic functions. RPS5 regulates MRPS5 expression and mitochondrial targeting, and this axis is required to sustain mitochondrial function, metabolic enzyme expression, and proteostasis under diabetic stress. **(A)** Representative Western blot analysis of MRPS5 protein expression in

cardiomyocytes following RPS5 overexpression or knockdown. Empty vector and negative control siRNA served as respective controls (n = 3). β-actin was used as a loading control. The bottom panel shows quantification of MRPS5 protein levels. **(B)** Representative immunofluorescence images showing the subcellular localization of MRPS5 (green) and mitochondria (Mito-tracker, red) in cardiomyocytes with or without RPS5 overexpression. Nuclei were counterstained with Hoechst (blue) (n = 6). Scale bars, 20 μm. Merged images and intensity profile plots along the indicated linear region of interest reveal enhanced colocalization of MRPS5 with mitochondria upon RPS5 overexpression. Pearson's correlation coefficient (r = 0.85) quantifies the degree of colocalization. **(C)** Representative Western blot analysis of MRPS5 protein expression in mitochondrial fractions isolated from cardiomyocytes following RPS5 overexpression or knockdown (n = 3). COX IV served as a mitochondrial loading control. The bottom panel shows quantification of mitochondrial MRPS5 protein levels. **(D)** Mitochondrial respiratory function was assessed by Seahorse extracellular flux analysis in cardiomyocytes under the indicated experimental conditions. Oxygen consumption rate (OCR) was measured over time following sequential injections of oligomycin, FCCP, and rotenone/antimycin A (n = 4). The bottom panel shows quantification of basal and maximal respiration rates. **(E)** Representative Western blot analysis of oxidative phosphorylation (OXPHOS) complex subunits, including ATP5A (Complex V), UQCRC2 (Complex III), MTCO1 (Complex IV), SDHB (Complex II), and NDUFB8 (Complex I), in HG+PA-treated cardiomyocytes with RPS5 overexpression alone or combined with MRPS5 knockdown (n = 3). β-actin served as a loading control. **(F)** Quantification of OXPHOS subunit protein levels corresponding to (E). **(G)** Representative Western blot analysis of metabolic enzyme expression, including glycolysis-related enzymes (HK1, G6PD, FBP2), fatty acid oxidation-related enzymes (CPT2, GPD1, ACOX1), and amino acid metabolism enzymes (HADH, FAH, IDO1), in HG+PA-treated cardiomyocytes with RPS5 overexpression alone or combined with MRPS5 knockdown (n = 3). β-actin served as a loading control. Under HG+PA conditions, RPS5 overexpression upregulated multiple metabolic enzymes, an effect that was abrogated by MRPS5 knockdown. **(H)** Representative immunofluorescence images of Thioflavin T (ThT) staining (green) detecting protein aggregates in HG+PA-treated cardiomyocytes with RPS5 overexpression alone or in combination with MRPS5 knockdown. Nuclei were counterstained with DAPI (blue) (n = 6). Scale bars: 100 μm. **(I)** Representative immunofluorescence images showing endoplasmic reticulum (ER) morphology in HG+PA-treated cardiomyocytes stained with ER-Tracker (green) and nuclei counterstained with Hoechst (blue) under the indicated conditions (n = 6). Scale bars: 5 μm. **(J)** Representative immunofluorescence images of JC-1 staining assessing mitochondrial membrane potential (ΔΨm) in HG+PA-treated cardiomyocytes under the indicated conditions (n = 6). Scale bars: 20 μm. **(K)** Quantification of Thioflavin T fluorescence intensity (left panel), ER tubule percentage (middle panel), and JC-1 red/green fluorescence ratio (right panel) corresponding to (G), (H), and (I), respectively. Statistical significance was determined using the tests described in the Methods. All data are presented as mean ± SEM. *p < 0.05, **p < 0.01, and ***p < 0.001.